JKU
**JOHANNES KEPLER
UNIVERSITY LINZ**

Author

Angelina Kerschbaumer

Submission

Institute of Physical Chemistry and Linz Institute of Organic Solar Cells (LIOS)
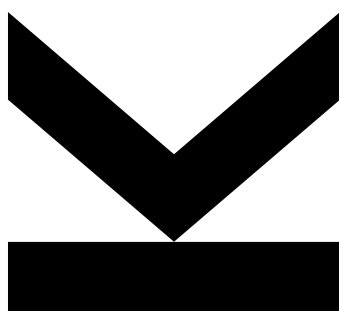
Thesis Supervisor

o.Univ. Prof. Mag. Dr. DDr. h.c. Niyazi Serdar Sariciftci

Co-Supervisor

DI Dominik Wielend

May 2022

ELECTROCATALYTIC OXYGEN REDUCTION TO HYDROGEN PEROXIDE USING ANTHRAQUINONE DERIVATIVES

Bachelor's Thesis

to obtain the academic degree of

Bachelor of Science (BSc)

in the Bachelor's Program

Chemistry and Chemical Technology

JOHANNES KEPLER

UNIVERSITY LINZ

Altenberger Straße 69

4040 Linz, Austria

SWORN DECLARATION

I hereby declare under oath that the submitted Bachelor's Thesis has been written solely by me without any third-party assistance, information other than provided sources or aids have not been used and those used have been fully documented. Sources for literal, paraphrased and cited quotes have been accurately credited.

The submitted document here present is identical to the electronically submitted text document.

Place, Date   Signature

Acknowledgement

There are many people whom I would like to thank for their contributions, both directly as well as indirectly, to this bachelor thesis. Foremost, I would like to express my deep and sincere gratitude to o. Univ.-Prof. Mag. Dr. DDr. h.c. Niyazi Serdar Sariciftci for arousing my interest in physical chemistry and giving me the opportunity to work at the Linzer Institute for Organic Solar Cells (LIOS).

Furthermore, I would like to acknowledge and give special thanks to my co-supervisor DI Dominik Wielend for his continuous support, guidance within this work and great advice. Thank you for introducing me into the field of electrochemistry, helping me with any upcoming question or problem and for the enthusiasm, wisdom as well as patience.

Additionally, I would like to thank the whole LIOS team for the warm welcome and for accepting me as an group member. Thank you for the often amusing and pleasant conversations during breaks making long, exhausting working days enjoyable. Working with such kind, supportive and knowledgeable colleagues was a major honor. I would like to thank especially Elisabeth Leeb, BSc and Nadine Kleinbruckner, BSc for the great cooperation during my work. A huge thanks also goes to Dr. Mihai Irimia-Vladu for the sublimation of several substances to purify those materials prior to any measurement.

Finally, my friends and family deserve a special mention for helping me survive the stressful time and not letting me give up. A big thanks to my boyfriend for the endless amount of love, support and encouragement to complete this thesis. My sincere thanks go to my family for supporting me throughout the years, financially and morally. I would also thank my friends for being so understanding and encouraging.

Abstract

Due to the rising demand of energy and the issues regarding fossil fuels, the interest in alternative energy, such as hydropower, wind or solar energy, has increased. However, the dependence of such renewable energy sources on several environmental factors, such as climate or season, causes fluctuations in the power production. Therefore, the research of storage systems has become essential. The storing of the excess energy enables the constant and uniform energy supply, even in times of higher consumption and less generation. Previous studies have shown that hydrogen peroxide (H_2O_2) can efficiently act as energy carrier. Hence, the aim of this thesis is to investigate the oxygen reduction towards H_2O_2 using various anthraquinone (AQ) derivatives as homogeneous electrocatalysts. Thereby, carbon electrodes were used to produce H_2O_2. After performing cyclic voltammetry (CV) for electrochemical characterization purposes, the rotating ring-disc electrode (RRDE) method as well as chronoamperometric measurements were used to qualitatively and quantitatively compare the H_2O_2 production of the different AQ compounds. Thus, the electrocatalytic behavior of those molecules was studied by two different approaches.

Kurzfassung

Aufgrund des steigenden Energiebedarfs und der Problematik bezüglich fossiler Brennstoffe ist das Interesse an alternativen Energien wie Wasser-, Wind- oder Solarenergie gestiegen. Die Abhängigkeit solcher erneuerbaren Energiequellen von mehreren Umweltfaktoren, wie Klima oder Jahreszeit, verursacht jedoch Schwankungen in der Stromproduktion. Daher ist die Erforschung von Speichersystemen unverzichtbar geworden. Die Speicherung der überschüssigen Energie ermöglicht eine konstante und gleichmäßige Energieversorgung auch in Zeiten höheren Verbrauchs und geringer Erzeugung. Frühere Studien haben gezeigt, dass Wasserstoffperoxid (H_2O_2) effizient als Energieträger fungieren kann. Das Ziel dieser Arbeit ist es daher, die Sauerstoffreduktion zu H_2O_2 unter Verwendung verschiedener Derivate des Anthrachinons (AQ) als homogene Elektrokatalysatoren zu untersuchen. Dabei wurden Kohlenstoffelektroden verwendet, um H_2O_2 zu erzeugen. Nach der Durchführung von Cyclovoltammetrie (CV) zur elektrochemischen Charakterisierung wurden die Methode der rotierenden Ringscheibenelektrode (RRDE) sowie chronoamperometrische Messungen verwendet, um die H_2O_2-Produktion der verschiedenen AQ-Verbindungen qualitativ und quantitativ zu vergleichen. Das elektrokatalytische Verhalten dieser Moleküle wurde somit anhand zweier unterschiedlicher Ansätze untersucht.

Table of Contents

1. Introduction

The scarcity of fossil fuel reserves, environmental concerns, oil price volatility and the increase in energy demand have lead to the growing importance of alternative and renewable energies [1,2]. Although the use of clean, renewable energy sources, including wind or solar energy, seems to be a promising option, their dependence of the power production rates on circumstances, such as weather, climate or season, has to be considered. For ensuring the reliability as primary energy sources, the energy of such alternative resources has to be stored. Hence, energy storage has gained in significance. By storing the generated surplus energy, the fluctuations in demand and the changing supply can be balanced [1]. Besides hydrogen, also hydrogen peroxide (H_2O_2) is a very efficient and clean fuel. The energy carrier H_2O_2 can be produced via the electrocatalytic two-electron oxygen (O_2) reduction and is used in fuel cells to generate electricity [3].

In the upcoming introductory chapters, the production processes and uses of H_2O_2 are summarized and the electrosynthesis of H_2O_2 via the oxygen reduction reaction (ORR) is further described. Moreover, the rotating ring-disc electrode (RRDE) method for analyzing the ORR towards H_2O_2 is discussed and chapter 1.5. provides an overview of anthraquinone (AQ) derivatives used within this work.

1.1. Applications of hydrogen peroxide (H_2O_2)

Hydrogen peroxide (H_2O_2) is a colorless liquid, completely miscible with water as well as soluble in some organic solvents [4]. Its weak acidity in aqueous solutions ($pK = 11.75$ at 20°C) leads to the ability of forming salts with different metals [4,5]. Additionally, H_2O_2 can either act as oxidant or reductant [4–6]. However, it is only capable of reducing strong oxidizing agents, such as potassium permanganate ($KMnO_4$) [6,7]. As water (H_2O) is the only produced byproduct of its oxidation, H_2O_2 is regarded as a green oxidizing agent [7–10]. Due to the low molecular weight (34.02 g mol^{-1}), H_2O_2 is considered to have a higher efficiency as oxidant than many others, including sodium hypochlorite (NaClO) or nitric acid (HNO_3) [7].

H_2O_2 has a broad range of applications, not only in areas of industry but also for domestic use [9–11]. Figure 1 gives a coarse overview of the possible application fields.
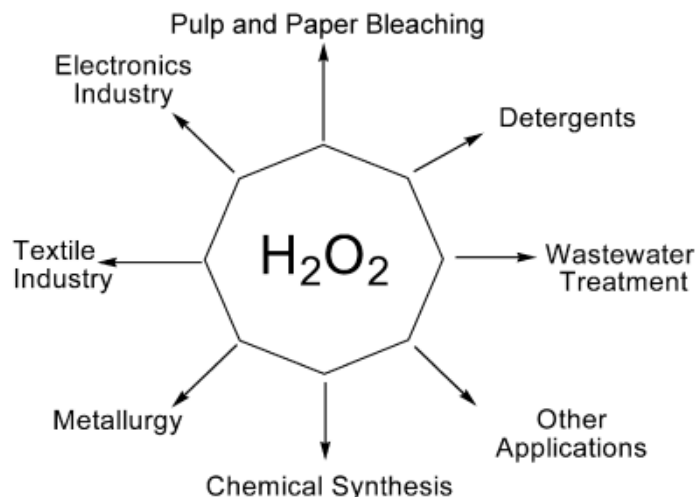
Figure 1: Different ranges of application of H_2O_2, reproduced from Dittmeyer *et al.* [8].

A major application of H_2O_2 is the use for paper and pulp bleaching purposes [4,7,9–11]. The replacement of chlorine-based bleaching agents by H_2O_2 reduces the amount of halogenated products found in waste streams [7]. Moreover, H_2O_2 is also used to bleach textiles. Compared to other bleaching agents in the textile industry, such as sodium hydrosulfite ($Na_2S_2O_4$), H_2O_2 is non-toxic and implies no severe effluent issues [7]. H_2O_2 is also efficiently applicable as disinfectant in medicine [4,9,12].

In addition, urban waste water is often treated with H_2O_2 in order to remove hydrogen sulfide (H_2S) that is formed in drains [7,13]. The H_2O_2 treatment of industrial waste also minimizes the amount of unwanted or toxic compounds, including organic matter, cyanide and thiocyanate [14]. As a source of the oxidizing hydroxyl radicals, H_2O_2 is used for the oxidation and inherent removal of toxic odorous gases in waste, such as nitrogen oxide (NO_x) gases [7]. Chemical oxidation with H_2O_2 is also used for the biological soil remediation to treat contaminants. Thereby, H_2O_2 can either directly oxidize or it generates oxidizing free-radicals by the catalytic decomposition of H_2O_2. The ions and metals of various transition metals, like iron (Fe), which are present in soil serve as catalysts for the formation of those radicals [15]. Furthermore, H_2O_2 can act as a oxygen source, for treating bulking sludges or in settling tanks to prevent denitrification [7].

Another application of high-concentrated H_2O_2 (60 to 100 weight percent) is the use as rocket propellant. H_2O_2 is applicable as monopropellant or as oxidant for bipropellants. Due to its high density, low viscosity, high boiling point and non-toxicity, H_2O_2 seemed to be a promising propellant [6,16]. In fact, H_2O_2 has a long history in propulsion applications. After a considerable research work in the era around the second world war, the Germans used the produced H_2O_2 for various weapons like the Messerschmidt Me 163, the first piloted rocket airplane, during the war. While the Allied Control Commission banned the synthesis of concentrated H_2O_2 in Germany, the development work has been continued in England as well as in the United States [6]. Nowadays more effective propellant alternatives with better performances exist. For instance, hydrazine-type fuels are frequently used due to its lower decomposition rate and high specific impulse [17,18].

Moreover, H_2O_2 serves as a reactant for chemical synthesis to reduce the environmental footprint of the chemical industry [7,13,19]. Oxidation processes relying on stochiometric oxidants, including permanganates, periodates or osmium oxide, are partly responsible for environmental pollution. H_2O_2 has a high potential for the use as eco-friendly oxidant for synthesizing fine and bulk chemicals. Therefore, those less environmentally friendly oxidizing agents are gradually replaced

by the green H_2O_2. Two major chemicals that are currently produced with the use of H_2O_2 are the large-volume substances propylene oxide and ε-Caprolactam [7].

Furthermore, H_2O_2 can be used in fuel cell technologies where chemical energy is converted into electrical energy. Thereby, it acts as a low-cost, environmentally friendly and easy to handle fuel to generate electricity. Hence, H_2O_2 is a promising alternative to other energy carriers like oil or H_2. Due to its ability of simultaneously acting as reductant and oxidant, H_2O_2 can be even operated in one-compartment cells [3,10,20]. Although the membrane-less structure of a one-compartment cell would reduce the costs of a fuel cell, such cells proved to have a low efficiency by achieving low voltages resulting in low output power. Therefore, the use of a large-scale H_2O_2 one-compartment cell requires research work to improve its performance [3,20,21].

Despite the already mentioned benefits of H_2O_2, there are some disadvantages. If spilled on combustible materials or on certain clothing, a danger of fire arises. This issue can be easily reduced by using appropriate protective equipment and by wearing Dacron or dynel fabrics which will not be ignited when in contact with H_2O_2 [6]. Furthermore, H_2O_2 contacting the skin causes white spots on the skin and vacuolar eruptions that disappear over time. This skin reaction can be explained by the diffusion of H_2O_2 into the affected area which results in the formation of O_2 due to the degradation of H_2O_2. Hence, it should be immediately flushed away with H_2O but the contact with low concentrated H_2O_2 does not lead to any severe long-lasting and painful injuries [6,22,23]. Another problem might be the contamination-dependent decomposition of H_2O_2. A large amount of contaminants increases the decomposition rate that results in a higher heat release and O_2 evolution rate. In addition to impurities, also the temperature and the peroxide concentration influence the rate of decomposition. However, by using suitable stabilizers and by properly cleaning, this disproportionation is minimized and H_2O_2 is storable for years [6,7]. Hence, the dangers regarding the handling and storing of H_2O_2 can be controlled and avoided with safety regulations.

1.2. Production processes of H_2O_2

In 1818, Thénard was the first one to synthesize H_2O_2 by acidifying barium peroxide (BaO_2) using HNO_3 [5,7,24]. The improved process of wet chemical oxidation with the use of hydrochloric acid (HCl) instead of HNO_3 was established in 1880 [5,25]. The first electrochemical production of H_2O_2 using sulphuric acid (H_2SO_4) was introduced by Meidinger in 1853 [26]. In 1878, Berthelot showed the formation of peroxodisulphuric acid ($H_2S_2O_8$) in the first electrolysis step of H_2SO_4. The hydrolyzation of this intermediate with H_2O yields peroxomonosulphuric acid (H_2SO_5) which gets further hydrolyzed to synthesize H_2O_2 and to re-obtain H_2SO_4 [4,5]. In Weissenstein (Austria), the first electrochemical production plant, based on the electrolytic process, was built in 1908 [4,25]. Another significant milestone was accomplished by Manchot who reported in 1901 the selective H_2O_2 production by reacting various organic molecules, including hydroquinones and hydroazobenzenes, with O_2 under alkaline conditions [13,27]. Due to the development of the antraquinone auto-oxidation (AO) process in 1939, Riedl and Pfleiderer have laid the foundation stone for the large-scale industrial production of H_2O_2 [28]. In the 1940s the first commercial AO process plant was built in Germany by IG Farbenindustrie [7,12].

The anthraquinone (AQ) process involves two major steps which are shown in Scheme 1.
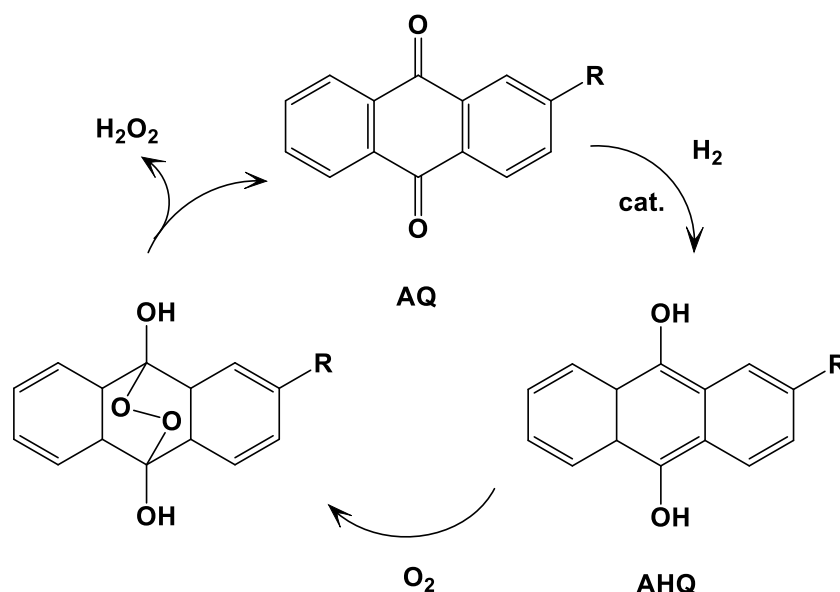
Scheme 1: Reaction scheme of the AO process with the hydrogenation of an alkylated AQ, formation of an endoperoxo complex as well as the auto-oxidation of AHQ to AQ, R corresponds to an alkyl group. Scheme adapted from Nishimi *et al.* [9].

At first, at elevated temperatures an alkylated AQ dissolved in an appropriate solvent is reduced to the respective anthrahydroquinone (AHQ) with hydrogen gas (H_2) using a catalyst [4,5,7]. Typically used catalysts are palladium (Pd) or nickel (Ni) [4,13,29,30] and the reaction is performed under a H_2 partial pressure of about 4 bars [5,7]. After this hydrogenation process, the catalyst is removed to avoid decomposition of H_2O_2 [4] and the auto-oxidation process under mild conditions follows. Thereby, AHQ is non-catalytically re-oxidized to AQ using oxygen (O_2) by bubbling air through the reaction solution [4,5,7,9,13]. An endoperoxo complex is formed as an intermediate [9]. As a result of this oxidation, H_2O_2 is simultaneously formed and can be separated and purified. For the completeness of the cycle, the re-obtained AQ is returned back to the hydrogenator and reused [4,7,9]. The AO production process is very selective (over 99.96 % per cycle [4]) and a high yield is obtained [4,7,9,29].

Despite the high yield and selectivity per cycle, there are various drawbacks regarding the AO process. A disadvantage within this process is the expensive separation and purification of the produced H_2O_2. The production of H_2O_2 via the AO method is only economically feasible in a large-scale because it entails high operating and capital costs [5,31]. An additional issue is the use of high amount of solvents or complex solvent systems that are toxic [31]. Extremely oxidizing conditions lead to the potential oxidization of AHQ to the corresponding epoxide. Hence, a constant AQ replenishment is necessary to enable a satisfactory yield of H_2O_2 [7,13]. Furthermore, this batch process involves safety risks because of the large amount of concentrated liquid H_2O_2 that has to be transported and stored [10,13]. Besides the aerospace industry (see chapter 1.1.), only few application fields require H_2O_2 in the highly concentrated form [10]. Moreover, explosive organics-air mists are generated that cannot be avoided by correlating the pressure and/or temperature [4]. Due to the energetic inefficiency, the AO method cannot be regarded as green [5,7]. Nevertheless, the main production process of H_2O_2 is still based on the AO [7,8]. However, because of the shortcomings concerning the AO process researchers focus on finding economical, energy-efficient and environmentally friendlier methods of producing H_2O_2.

Alternatively, H_2O_2 can be produced via the small-scale direct synthesis involving the reaction of H_2 and O_2 in a solvent in the presence of a Pd or gold (Au)-Pd catalyst [5,7,10,13]. Since its development in 1914 [32], the direct reaction method seems to be a promising alternative technology that has gained in interest [5,10,13,31]. However, this direct route requires the handling of H_2/O_2 mixtures that are potentially dangerous as explosive mixtures range between 4 to 94 mol% (H_2 in O_2 at 1 atm) [8]. Therefore, an inert carrier gas like carbon dioxide (CO_2) is required to dilute the reactants. This dilution and the inherent side reactions minimize the yield of H_2O_2 [7,8,10,13]. An additional green alternative, on which considerable research is currently done, is the electrochemical production of H_2O_2 via the selective reduction of O_2 [5,10,33]. In this process, the formation of explosive mixtures can be avoided by keeping H_2 and O_2 separated or by using a different proton source than H_2 [5,34]. Additionally, the electrosynthesis is not only practical on small but also on large scales and is regarded as cost-effective [10]. Moreover, the performance of the H_2O_2 production inside a electrolysis cell allows the recovery of the thereby released energy [33]. However, there are various competing reactions associated with the H_2O_2 generation via the oxygen reduction [10,33]. Thus, one research challenge of the electrochemical production method is to find electrocatalysts and electrode materials which favor the selective two-electron reduction of O_2 towards H_2O_2 [5,10,33]. Whereas noble metals, such as platinum (Pt) [34], prefer the 4-electron pathway, metal alloys, like Pd-Au [13], also (doped) carbon [35] and transition metal catalysts, including cobalt (Co) [36], can be used as electrocatalyst for the 2-electron reduction of O_2 [10,33]. Not only the catalyst material but also the reactor design and the form as well as geometry of the electrode are significant for obtaining an optimal yield [10,34]. This process is described in more detail in chapter 1.3.

1.3. Electrochemical oxygen reduction reaction (ORR)
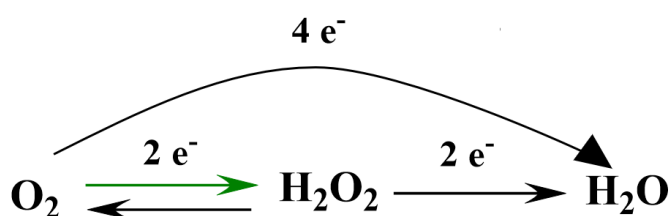
Scheme 2: Reactions occurring within the O_2 reduction.

The before mentioned (chapter 1.2.) O_2 reduction reaction (ORR) involves several reactions that are summarized in Table 1 and schematically displayed in Scheme 2. There is not only the 2-electron reduction pathway (Eq. 1+Eq. 4) which is desired for the electrochemical H_2O_2 production but also the 4-electron reduction reaction towards water (H_2O) (Eq. 2+Eq. 5). Additionally, the formed H_2O_2 can be further reduced to H_2O (Eq. 3+Eq. 6) [10,37,38].

Table 1: Summary of reactions involved in ORR with the respective thermodynamic electrode potentials [38].

Electrolyte	ORR reaction	E^0	
	$O_2 + 2e^- + 2H^+ \rightarrow H_2O_2$	$0.70\ V$	(Eq. 1)
Acidic aqueous solution	$O_2 + 4e^- + 4H^+ \rightarrow 2H_2O$	$1.229\ V$	(Eq. 2)
	$H_2O_2 + 2H^+ + 2e^- \rightarrow 2H_2O$	$1.76\ V$	(Eq. 3)

Alkaline aqueous solution	$O_2 + 2e^- + 2H_2O \rightarrow HO_2^- + OH^-$	$-0.065\,V$	(Eq. 4)
	$O_2 + 4e^- + 2H_2O \rightarrow 4OH^-$	$0.401\,V$	(Eq. 5)
	$HO_2^- + H_2O + 2e^- \rightarrow 3OH^-$	$0.867\,V$	(Eq. 6)

The interaction between O_2 and the catalyst/metal electrode surface (*) influences the ORR process. Therefore, the reaction pathway of these reactions depends on the surface of the material. As illustrated in Figure 2, there are two different ways how O_2 can adsorb on active binding sites. One way would be the side-on adsorption where the binding of both O-atoms to a metal site hinders the leaving of H_2O_2 intermediates and leads to the further reduction to H_2O. Alternatively, O_2 adsorbs end-on with only one O-atom bound to the electrode material. This adsorption type is favorable for the 2-electron reduction yielding H_2O_2 as product [10,34].
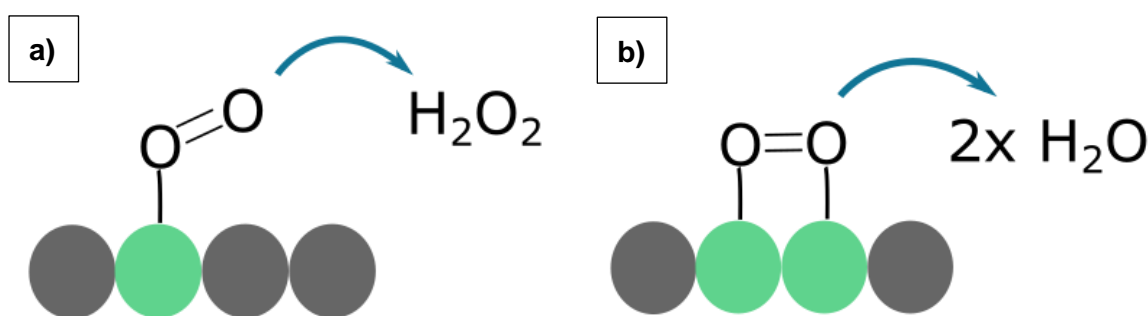
Figure 2: Depiction of a) the end-on adsorption of O_2 yielding H_2O_2. b) the side-on adsorption of O_2 yielding H_2O. Adapted from Perry *et al.* [10].

The respective binding intermediate steps of the two reduction pathways are listed below. Concerning the 4-electron O_2 reduction one has to differentiate between the associative and dissociative mechanism. In the associative mechanism the dissociation of O_2 occurs after the hydrogenation. In contrast to this, in the dissociative process the oxygen-oxygen (O-O) bond already breaks upon the adsorption of O_2 yielding *O [34,37,39]. As the associative mechanism also allows the formation of H_2O_2 instead of H_2O, it is additionally named peroxo mechanism [39].

In addition to the O_2 binding orientation, also the interaction strength has an impact on the reduction pathway. Electrode materials donating a high electron density to O_2 result in stronger metal-oxygen (M-O) bonds. This strong bonding slows down the catalytic turnover and promotes the 4-electron reduction towards H_2O. For the selective H_2O_2 synthesis via the 2-electron reduction of O_2 an electrode material on which the generated H_2O_2 is only weakly bound is necessary. Thereby, H_2O_2 can dissociate as final product before undergoing further reduction or oxidation [10]. Besides many other available electrode materials, carbon-based electrodes have a good performance with respect to the cathodic electrosynthesis of H_2O_2 [10]. The selectivity towards the H_2O_2 formation can be even more increased when using porous structures that enhance mass transport [10,35]. Porous (carbon) electrodes have high surface areas, allow a valid mass transport and favor the 2-electron O_2 reduction because of the higher number of defect sites [10]. Park *et al.* reported that especially the mesoporous structure of the material shows a promising effect. Hence, the control of this mesoporous structure is significant for the improvement of the catalytic activity and selectivity [35]. Furthermore, Choi *et al.* demonstrated that Pt catalysts coated with amorphous

carbon favor the end-on adsorption of O_2. By eliminating the accessible active adsorption sites, the selectivity of the H_2O_2 formation is enhanced. The amorphous layers suppress the side-on adsorption as well as the subsequent reduction of H_2O_2 towards H_2O. The formed H_2O_2 has no access to the embedded Pt surface which leads to the suppression of the further decomposition reaction [34]. Not only the structure, but also the composition of the surface or bulk can be tuned to increase the H_2O_2 production. Due to chemical effects of the doping materials, the electrode activity towards the 2-electron O_2 reduction can be improved [10].

In addition to inorganic materials, also organic electrocatalysts exist and can efficiently drive the selective O_2 towards H_2O_2 reduction reaction. For instance, quinone modified carbon electrodes have been reported a lot and show a high electrocatalytic activity. Due to the increase of the reduction rate of O_2, the kinetic investigation of the O_2 reduction using quinone-modified carbon electrodes has become a significant area of research [40–44] . With the attachment of quinones the 2-electron reduction is enhanced, as the peroxide is the dominant final product [41,42]. The rotating ring-disc electrode (RRDE) technique can be employed for the study of those electrodes (see chapter 1.4.). For instance, a recent RRDE study of anthraquinone 2-sulfonate (AQS) by Wielend *et al.* revealed the electrocatalytic behavior of homogeneous aqueous AQS solutions [45].

Further research work regarding catalytic O_2 reduction to H_2O_2 has been performed at the Linz Institute for Organic Solar Cells (LIOS). For example, riboflavin homogeneously dissolved in aqueous solution was identified as electrocatalyst [46] and carbon electrodes modified with conducting polymers, like polypyrrole, proved to catalyze the H_2O_2 production [47]. Apaydin *et al.* demonstrated photoelectrocatalysis using electrodes consisting of titanium dioxide (TiO_2) coated with molecular copper-porphyrin [48]. Additionally, Jakešová *et al.* reported semiconductor photoelectrodes that yield a high amount of produced H_2O_2 [49].

Moreover, the electrosynthesis of H_2O_2 can also proceed via the 2-electron oxidation of H_2O according to Eq. 7 [10].

$$H_2O \rightarrow H_2O_2 + 2e^- + 2H^+ \qquad E^0 = 1.760\,V \qquad \text{(Eq. 7)}$$
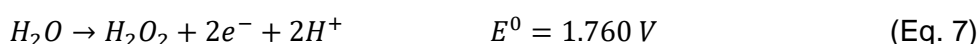
However, this is not the target reaction within this thesis. Hence, the H_2O_2 generation by oxidizing H_2O will not be mentioned in any further detail.

1.4. Rotating Ring-Disc Electrode (RRDE) technique

During the cold war, the first hydrodynamic voltammetry with the use of rotating electrodes was developed in Russia. In 1952, Levich published a book in which the mass transport to the surface of such a rotating disc electrode (RDE) was explained [50]. The solution flux towards the surface of the disc is independent of the radial distance from the rotation axis. Thus, the mass transport theory for RDEs was established using simple mathematics. The reduction of an electroactive species (A) at a RDE with n_D electrons involved can be described with a cathodic half-reaction shown in Eq. 8 [51].

$$A + n_D e^- \rightarrow B \qquad \text{(Eq. 8)}$$
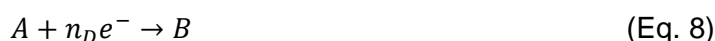
The rotation of a RDE leads to the movement of the species A towards the electrode due to convection. This reduction of A at the disc and the inherent formation of B can be seen in the schematic linear sweep voltammogram (LSV) in Figure 3b. Additionally, at a certain negative potential of the electrode a steady-state condition is observable [51]. Thereby, a constant limiting disc current ($I_{D,lim}$) is obtained and can be determined using the Levich equation (Eq. 9) [51–54].

$$I_{D,lim} = 0.62n_D F\pi r_D{}^2 c_A D_A{}^{2/3} v^{-1/6} \omega^{1/2}$$

(Eq. 9)

As shown in Eq. 9, this $I_{D,lim}$ depends on the number of transferred electrons (n_D), the Faraday constant (F), the radius of the disc electrode (r_D), the initial concentration of the electroactive species A (c_A), the diffusion coefficient of A (D_A) and on the rotational speed (ω) [51].
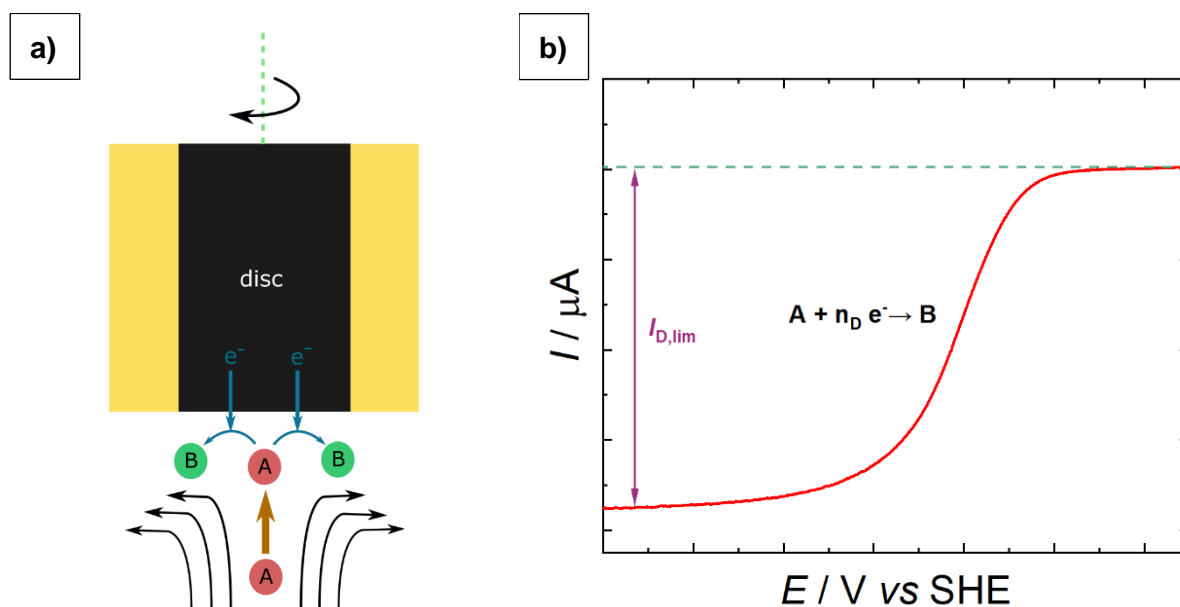

Figure 3: a) Depiction of the reduction of the electroactive species A into B at an RDE. b) Schematic LSV graph of this reduction at the disc electrode with the limiting disc current $I_{D,lim}$. Adapted from Wielend [55].

Levich`s establishment of the RDE was fundamental because it enabled the simple controllability of the rate of the electroactive species arriving at the surface of the electrode. In 1957, Levich developed together with Koutecký a further description of the overall disc current (I_D). This Koutecký-Levich-equation (Eq. 10) considers not only the mass transport to the disc surface but also the rate of the half-reaction [34,51,53].

$$\frac{1}{I_D} = \frac{1}{I_K} + \frac{1}{0.62n_D F\pi r_D{}^2 c_A D_A{}^{\frac{2}{3}} v^{-\frac{1}{6}} \omega^{\frac{1}{2}}}$$

(Eq. 10)

The right part of Eq. 10 corresponds to the mass transport limited contribution to the current, whereas the left part describes the kinetic current (I_K) which is the current flowing without any mass transport limitations [51,55]. Therefore, the Koutecký-Levich-equation can be used to determine, for example, I_K. For this, RDE measurements with different rotation rates have to be performed. As the disc current is dependent on the rotational speed, the reciprocal of the measured current ($1/I_D$) can be plotted against the reciprocal of the square root of the rotation rate ($\omega^{1/2}$). The intercept of this plot corresponds then to $1/I_K$ [51].

In 1958, the idea of a rotating ring-disc electrode (RRDE) was invented by Frumkin. In a RRDE system, the additional concentric ring electrode surrounding the disc electrode allows the collection of electrochemical intermediates that were generated at the disc [51]. Figure 4b shows an exemplary LSV graph of a RRDE experiment where the disc potential is swept while keeping

a constant anodic potential at the ring. The schematic depiction of such a RRDE system is displayed in Figure 4a.
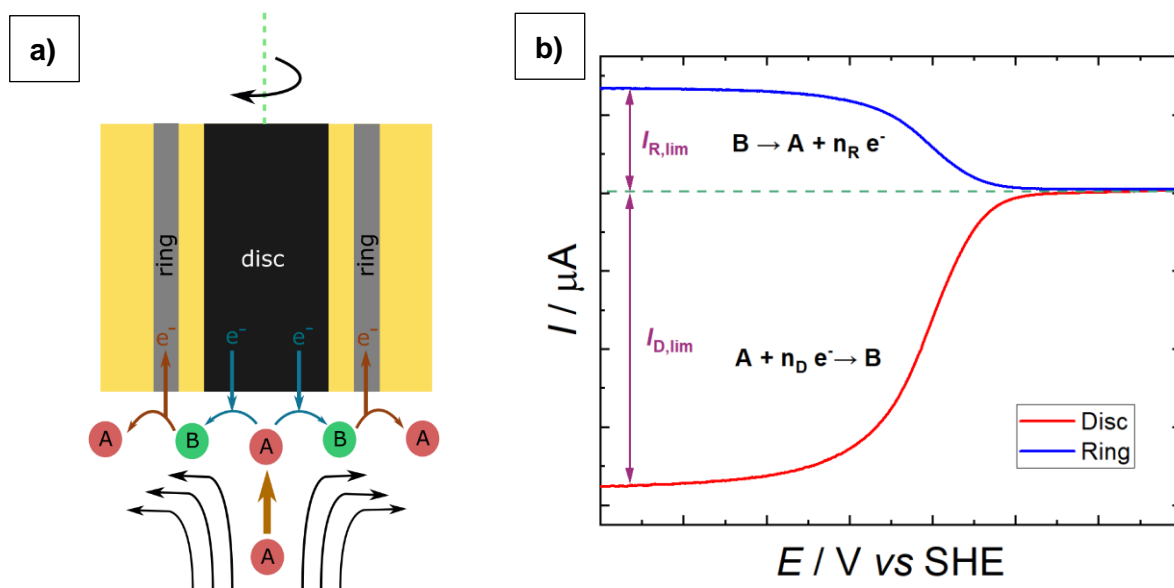

Figure 4: a) Depiction of the electrochemical process at an RRDE with the reduction of the electroactive species A into B at the disc and the re-oxidation of B into A at the ring. b) Schematic LSV graph of this reduction at the disc electrode with the limiting disc current $I_{D,lim}$ and the back oxidation at the ring with the limiting ring current $I_{R,lim}$. Adapted from Wielend [55].

Assuming again the reduction reaction of A to B (Eq. 8) at the disc, the anodic half-reaction of the re-oxidation of B to A at the ring can be described using Eq. 11.

$$B \rightarrow A + n_R e^-$$ (Eq. 11)

One must consider that the number of electrons involved in the ring half-reaction (n_R) is not always in accord with n_D. Due to the mass transport, some of the generated product B is moved towards the ring. However, most of the formed B is actually swept away. Thus, only a fraction of the products formed at the disc is collected at the ring. This fraction, also called maximum collection efficiency (N_{max}), is a significant dimensionless parameter for RRDE measurements [51,53]. If the needed RRDE dimensions are known, this N_{max} can be calculated via direct computation [51,56]. Instead of using numerical calculations, N_{max} can also be experimentally determined using a reversible redox system, such as Fe^{3+}/Fe^{2+}. For this, LSV measurements are conducted over a range of several rotation speeds using a solution of the respective reducible material, like potassium ferricyanide (III) ($K_3[Fe(CN)_6]$). As a result, N_{max} is obtained using the measured currents according to Eq. 12 [54–57].

$$N_{max} = \frac{I_{R,lim}}{|I_{D,lim}|}$$ (Eq. 12)

Additionally, during the re-oxidation of $B \rightarrow A$ a positive current at the ring is measured. Similar to the disc, also the ring current yields a limiting anodic current ($I_{R,lim}$) at a certain potential. Therefore, Eq. 13 is used to describe this $I_{R,lim}$ [51].

$$I_{R,lim} = -I_{D,lim}(\frac{n_R}{n_D})N_{max}$$ (Eq. 13)

Furthermore, as it can be seen in Figure 4b, the limiting current $I_{R,lim}$ has a much lower absolute value compared to $I_{D,lim}$. This difference can be again explained by the limitation of N_{max}.

The RRDE system is a powerful technology to investigate the electrocatalytic H_2O_2 production via the ORR. With the help of a catalyst, O_2 is reduced at the disc electrode. The rotation radially transfers the generated H_2O_2 to the ring electrode where it is re-oxidized to O_2. As a result, the faradaic efficiency (FE) for this H_2O_2 synthesis can be calculated according to Eq. 14 [5,55].

$$FE(\%) = \frac{I_R/N_{max}}{|I_D|} \cdot 100 \qquad \text{(Eq. 14)}$$

In addition, the corresponding number of transferred electrons (n) at the disc can be determined as follows [33,34,55,56] :

$$n = \frac{4\,|I_D|}{|I_D| + I_R/N_{max}} \qquad \text{(Eq. 15)}$$

1.5. Anthraquinone derivatives

In Figure 5, the unsubstituted structure of an AQ can be seen. This molecule is characterized by a fused three-ring aromatic system with ketone functionalities at the positions 9 and 10.
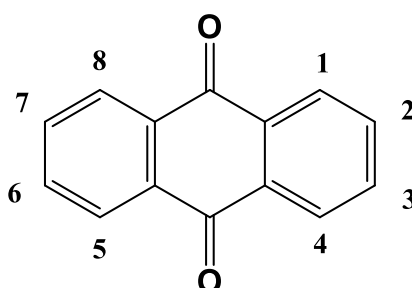
Figure 5: General structure of an AQ.

There are various derivatives with different functional groups possible and available. However, only a few hydroxy-substituted and sulfonated AQ compounds are considered and used within this work. These are 1-Hydroxyantraquinone (1-OH-AQ), 2-Hydroxyantraquinone (2-OH-AQ), 1,2-Dihydroxyantraquinone (1,2-OH-AQ), 1,4-Dihydroxyantraquinone (1,4-OH-AQ), Alizarin Red S (ARS) and sodium anthraquinone 2-sulfonate monohydrate (AQS).

As already mentioned in chapter 1.2, those highly conjugated molecules are significant for the H_2O_2 synthesis via the AQ auto-oxidation process. Additionally, quinone compounds like AQ derivatives are also employed as catalysts for the electrochemical production of H_2O_2 by reduction of O_2 (see chapter 1.3). Several AQ compounds can shift the O_2 reduction potential to more anodic potentials which facilitates the reduction. The proposed reaction mechanism of the ORR with an AQ electrocatalyst is displayed below [41,58]. This mechanism resembles the H_2O_2 production via the AO process shown in Scheme 1 (chapter 1.2.).

$$AQ + 2e^- + 2H^+ \rightarrow AQH_2 \qquad \text{(Eq. 16)}$$

$$AQH_2 + O_2 \rightarrow AQ + H_2O_2 \qquad \text{(Eq. 17)}$$

The rapid redox kinetics and the chemical tunability of AQ derivatives makes them suitable for their application in flow batteries. The respective reduction potentials depend on the substitution of the AQ molecule [59–61].

Due to the anti-viral [62], immune-boosting [63] and anti-inflammatory [64] effectiveness of various AQ derivatives, they also find application as active agents against several viruses, such as HIV, influenza and herpes [65]. The current COVID-19 pandemic even lead to the research of the probable utilization of AQ compounds as immune-boosters against the corona virus [65]. Moreover, hydroxyanthraquinones, naturally occurring in various medicinal plants like aloe vera, are known for their laxative efficacy [66]. In spite of their pharmacological effects, there are some toxicity and mutagenicity concerns with regard to drugs containing AQs [66–69].

Furthermore, hydroxylated AQ pigments are used as (natural) dyes in the textile, food, cosmetic as well as paint industry. However, the already mentioned health hazards associated with some AQ derivatives have to be considered [70,71]. Hence, those colorants are mostly used in small amounts combined with further coloring substances [71].

2. Experimental

2.1. Materials and chemicals

All chemicals, solvents, gases and other materials which were used within this study are listed in Table 2. For further purification purposes, 1-OH-AQ, 2-OH-AQ, 1,2-OH-AQ and 1,4-OH-AQ were sublimed prior to usage.

Table 2: List of chemicals and materials used.

Material	Formula	Abbreviation	Supplier	Purity
Acetone	C_3H_6O	-	VWR Chemicals	≥99%
Acetonitrile	C_2H_3N	MeCN	Carl Roth	≥99.9%
Alizarin Red S sodium salt	$C_{14}H_7NaO_7S$	ARS	Alfa Aesar	powder
Alumina paste (1 µm)	Al_2O_3	Al_2O_3	Buehler	-
Alumina paste (0.3 µm)	Al_2O_3	Al_2O_3	Buehler	-
Alumina powder (0.05 µm)	Al_2O_3	Al_2O_3	Buehler	-
Anthraquinone	$C_{14}H_8O_2$	AQ	Sigma-Aldrich	97%
1,2-Dihydroxyanthraquinone	$C_{14}H_8O_4$	1,2-OH-AQ	Alfa Aesar	94%
1,4-Dihydroxyanthraquinone	$C_{14}H_8O_4$	1,4-OH-AQ	Sigma-Aldrich	≥98.0%

Dimethylsulphoxide	C_2H_6OS	DMSO	VWR Chemicals	99.7%
Disodium hydrogen phosphate	Na_2HPO_4	-	Sigma-Aldrich	≥99.0%
Glassy carbon plate 2 mm	-	GC	Alfa Aesar	Type 1
Ferrocene	$C_{10}H_{10}Fe$	Fc	Sigma-Aldrich	98%
Hydrogen peroxide	H_2O_2	H_2O_2	Merck	for synthesis, 30%
1-Hydroxyanthraquinone	$C_{14}H_8O_3$	1-OH-AQ	TCI Chemicals	>95.0%
2-Hydroxyanthraquinone	$C_{14}H_8O_3$	2-OH-AQ	Activate Scientific	95%
Iso-Propanol	C_3H_8O	IPA	VWR Chemicals	technical
4-Nitrobenzeneboronic acid	$C_6H_6BNO_4$	p-NBBA	Alfa Aesar	95%
Nitrogen	N_2	N_2	JKU houseline	-
Oxygen	O_2	O_2	Linde	5.0
Phosphoric acid	H_3PO_4	H_3PO_4	Sigma-Aldrich	99%
Platinum wire (∅ = 0.3 mm)	Pt	Pt	Ögussa	99.9%
Potassium chloride	KCl	KCl	Alfa Aesar	99%
Potassium hexacyanoferrate (III)	$K_3[Fe(CN)_6]$	$K_3[Fe(CN)_6]$	Sigma-Aldrich	99+%
Potassium hexacyanoferrate (II)	$K_4[Fe(CN)_6]$	$K_4[Fe(CN)_6]$	Merck	pro analysis
Riboflavin	$C_{17}H_{20}N_4O_6$	Rf	Sigma-Aldrich	≥98%
Silver wire (∅ = 0.5 mm)	Ag	Ag	ChemPur	99.9%
Sodium anthraquinone 2-sulfonate monohydrate	$C_{14}H_7NaO_5S·H_2O$	AQS	TCI Chemicals	>98.0%

Sodium carbonate	Na_2CO_3	Na_2CO_3	Fluka	≥99.5%
Sodium hydrogencarbonate	$NaHCO_3$	$NaHCO_3$	Alfa Aesar	99.7-100.3%
Sodium hydroxide	NaOH	NaOH	Merck	pellets for analysis
Sodium phosphate monobasic dihydrate	$NaH_2PO_4 \cdot 2H_2O$	-	Sigma-Aldrich	≥99.0%
Sulphuric acid	H_2SO_4	H_2SO_4	J. T. Baker	95-97 %
Tetrabutylammonium hexafluorophosphate	$C_{16}H_{36}F_6NP$	$TBAPF_6$	Sigma-Aldrich	for electrochem. analysis, ≥99.0%

2.2. Instrumentation

The instruments which were used in this work are summarized in Table 3. All measurements for electrochemical characterization purposes were performed using either an Ivium Vertex One.EIS, Potentiostat-Galvanostat PGU 10V - 100mA, Potentiostat-Galvanostat 1030 PC.T or a Bipotentiostat-Galvanostat PGU BI-1000.

Table 3: Used instrumentation.

Instrument	Name	Vendor
Analytical balance	Acculab Sartorius group	Acculab
Bipotentiostat	Bipotentiostat-Galvanostat PGU BI-1000	IPS Jaissle
pH-electrode	pH electrode HI1131	HANNA
Potentiostat	Potentiostat-Galvanostat PGU 10V - 100mA	IPS Jaissle
Potentiostat	Potentiostat-Galvanostat 1030 PC-T	IPS Jaissle
Potentiostat	Ivium Vertex One.EIS	Ivium
Rotation controller	IPS PI-ControllerTouch	IPS Jaissle
Rotator	IPS Rotator 2016	IPS Jaissle
UV-Vis spectrometer	Varian Cary 3G UV-Visible Spectrophotometer	Varian
UV-Vis spectrometer	Thermo Scientific Multiscan GO Spectrometer	Thermo Scientific

2.3. Electrode preparation

Depending on the measurement type, different working electrodes (WE) were used for the electrochemical characterizations. GC electrodes were used for CVs and electrolysis and GC/Pt electrodes for RRDE measurements. For the removal and avoidance of contaminations those electrodes were cleaned before usage. In the case of chronoamperometric experiments, the GC plates were not only polished but also activated prior to measuring.

2.3.1. Plate-type electrodes

2 mm thick 1 x 4 cm GC plates were used to perform electrolysis. For cleaning purposes, those plates were polished as well as electrochemically activated to obtain clean electrodes. The cleaning was conducted following the procedure described by Rabl [72] and Elgrishi *et al.* [73]. Thereby, the electrode was polished in an eight-shaped movement on a glass plate (Figure 6a). Deagglomerated alumina (Al_2O_3) pastes with decreasing particle sizes of 1.0, 0.3 and 0.05 µm were used for 1 min each. For the removal of excess alumina particles, the last polishing step was performed with a toothpaste. Between each change of paste, the electrodes were rinsed and ultrasonicated in 18 MΩ water and *iso*-propanol (IPA) for 10 minutes each.
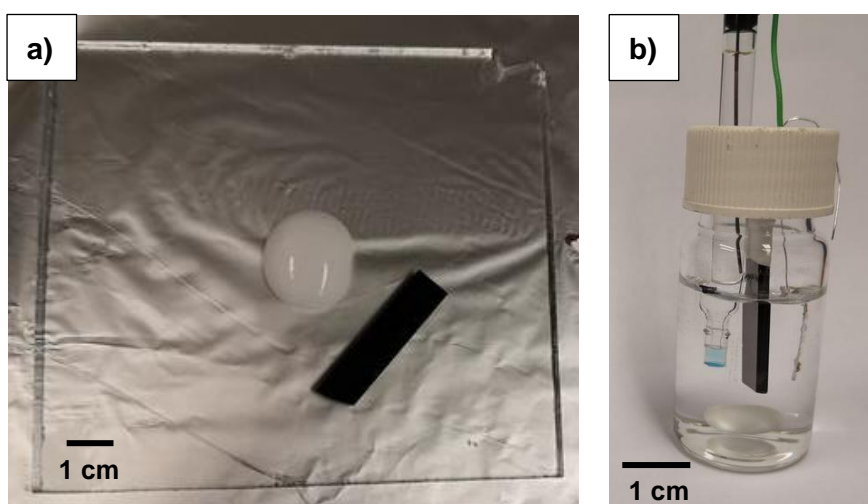
Figure 6: a) Polishing of a GC electrode on a glass plate with white Al_2O_3 pastes. b) One-compartment cell for the activation of the GC WE with an Ag/AgCl (3 M KCl) as RE and a Pt-foil as CE.

Afterwards, the electrode was electrochemically activated via a cyclic voltammetry (CV) in 0.5 M sulphuric acid (H_2SO_4). For this, an Ag / AgCl (3M KCl) reference electrode (RE) and a Pt-foil as counter electrode (CE) were used (Figure 6b). Starting at 0 V, the potential was then swept for 30 cycles between +1500 mV and -1000 mV at a scan rate of 50 mV s^{-1}. Figure 7 shows an exemplary graph for this electrode activation.
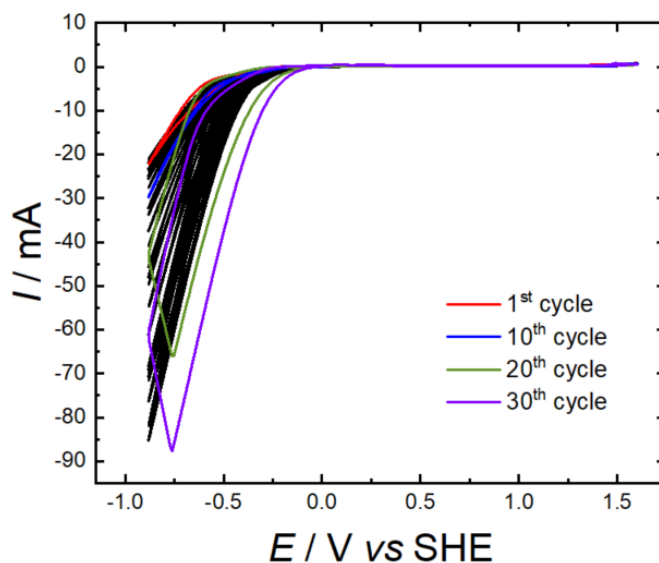
Figure 7: Activation graph of a GC plate electrode in 0.5 M H_2SO_4.

2.3.2. Disc-type electrodes

The disc-type electrodes, such as the GC disc electrode or the GC/Pt-RRDE were used for the standard CV and LSV measurements. Those electrodes also needed to be pre-treated before being used. For this, a similar polishing procedure as for the plate-like electrodes was conducted. The three Al_2O_3 pastes with decreasing particle sizes were used in decreasing order on a polishing pad for 30 sec each. Between the polishing steps, the electrode was rinsed with 18 MΩ water and IPA.

Additionally, the RRDE was further cleaned by immersion in 0.1 M NaOH for 30 min prior to each experiment.

2.4. Electrochemical characterization

2.4.1. Cyclic voltammetry

The used potentiostats for cyclic voltammetry experiments are listed in Table 3 (section 2.2.). All potentials stated in this work were referenced versus the standard hydrogen electrode (SHE). Measurements in an organic solvent were performed in a one-compartment cell with a 0.1 M solution of tetrabutylammonium hexafluorophosphate (TBAPF$_6$) in acetonitrile (MeCN). Those cells were filled with 10 mL of the electrolyte solutions, equipped with a cleaned 3 mm GC disc electrode (see section 2.3.1. for the cleaning procedure) as WE, a Pt-foil as CE and an Ag/AgCl quasi-reference electrode (QRE). The AQ derivatives soluble in MeCN were homogeneously dissolved to obtain 1 mM solutions. However, due to the lower solubilty, the concentration of the 2-sulfonate-antraquinone (AQS) in MeCN was only 0.5 mM. Figure 9b shows a schematic representation of such an electrochemical cell. In order to enable an inert environment, all measurements in MeCN were conducted in a glove box filled with nitrogen (N_2). After conducting the CV, the QRE was calibrated by adding ferrocene to the compartment and another CV was recorded. Therefore, the calibration versus ferrocene was determined according to Figure 8 [53,74,75].
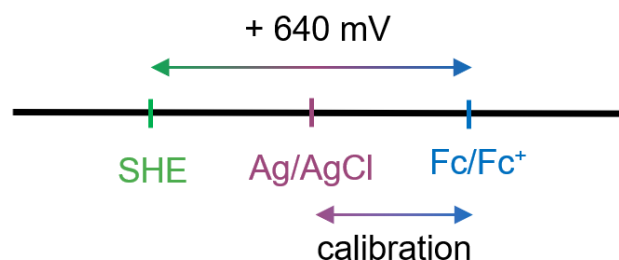
Figure 8: Graphical depiction of the conversion of the potential vs. Ag/AgCl QRE into a potential vs. SHE using a ferrocene calibration.

All experiments in aqueous media were performed either in 0.1 M NaOH solution with pH 13 or phosphate buffer (PB) with a pH of 2 or 7. The different solutions of the AQ derivatives were transferred into one-compartment cells with a 3 mm GC WE, Pt CE and an Ag/AgCl (3M KCl) RE (Figure 9). Before each electrochemical measurement, the cell was purged with either N_2 for 1 h or O_2 for 30 min. Due to the use of an Ag/AgCl (3M KCl) as RE, the measured potentials were recalculated via a calibration using potassium hexacyanoferrate (II) ($K_4[Fe(CN)_6]$). As a result, the potential reference versus SHE was achieved.
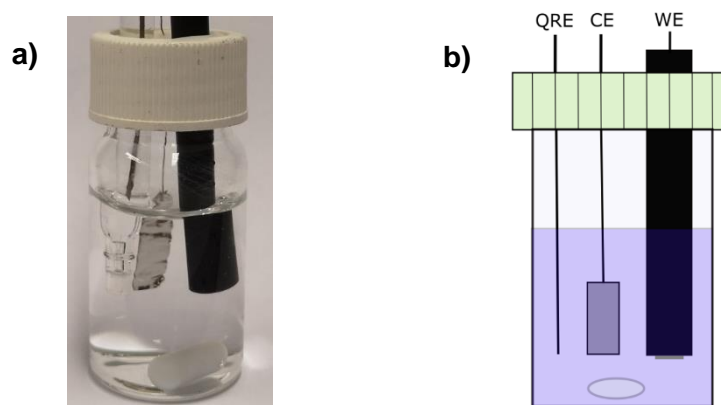
Figure 9: One-compartment cell with a disc-type GC WE, a Pt-foil as CE and a) an Ag/AgCl (3M KCl) RE for CV in aqueous media (photograph). b) an Ag/AgCl QRE for CV in organic media (schematic representation).

2.4.2. RDE and RRDE method

For the rotating (ring) disc experiments, not only a bipotentiostat but also a rotator with a rotation controller were necessary (see chapter 2.2.). The used setup is shown in Figure 10a.

Figure 10: a) Setup for RDE and RRDE measurements with the bipotentiostat, rotator as well as rotation controller. b) Purging an electrolyte solution in the glass compartment with the electrode attached to the rotator. c) Picture of the GC/Pt RRDE.

As rotating disc electrode (RDE) a Pt-disc with a diameter of 8 mm in poly(chlorofluoroethylene) (PTCFE) was used and the RRDE measurements were performed with a GC-disc and a Pt-ring in polyether ether ketone (PEEK) Figure 10c)). According to chapter 2.3.2., both electrodes were cleaned before each experiment. Besides the RDE or RRDE as WE, also a platinized CE and an Ag/AgCl (3M KCl) inside a Luggin capillary were used (Figure 10). Furthermore, 120 mL of the different electrolyte solutions were transferred into a glass cell which was further sealed and purged with N_2 or O_2 for 1 h. After achieving saturated conditions, the gas supply was continued in the headspace. At first, CVs were measured, followed by linear sweep voltammograms (LSV). The LSVs were recorded by applying a constant potential at the Pt-ring and after each voltammogram the rotational speed was increased. While the scan rate of 10 mV s^{-1} was always the same for all LSVs, the constant potential at the ring changed depending on the pH and material used. This ring potential was experimentally determined by the CV measurements before.

2.4.3. Chronoamperometry

All chronoamperometric measurements were performed using a Jaissle Potentiostat-Galvanostat, either a PGU 10V-100mA or a 1030 PC-T (see chapter 2.2.). Additionally, as shown in Figure 11 two-compartment cells with a clean and activated GC plate-type electrode as WE, a Pt-foil as CE and an Ag/AgCl (3M KCl) as RE were used. The WE side of the cell was filled with 35 mL of the respective 0.3 mM AQ solution in 0.1 M NaOH and a magnetic stirrer was added, whereas the CE compartment was filled with 40 mL of the 0.1 M NaOH solution. A Nafion membrane (117) separates the two sides. After flushing the cell with N_2 for 30 min, a CV was recorded. Then, both compartments were purged with O_2 for 30 min to ensure oxygen saturation. While the headspace of the WE side was further purged with O_2, the gas supply on the CE side was stopped. Another CV was measured before starting the electrolysis. During the whole 6 h of oxygen reduction electrolysis, the cell was magnetically stirred using a constant speed and a constant potential of -400 mV vs Ag/AgCl was applied. For the further determination of the amount of H_2O_2 produced, 100 µL aliquots of the electrolyte were taken from the WE side prior to the electrolysis as well as after 1, 2, 4 and 6 h. The procedure of quantifying the H_2O_2 is described in chapter 2.4.4.
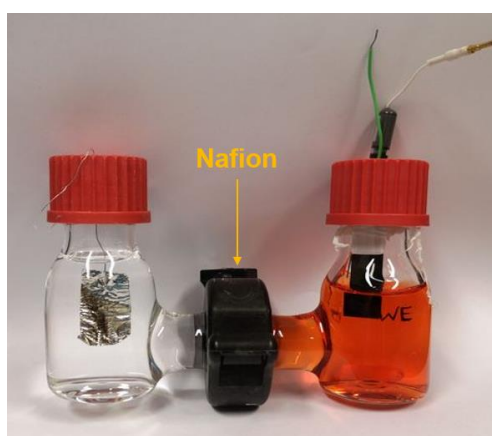
Figure 11: Two-compartment cell with a Nafion 117 membrane separating the left side containing a Pt-foil as CE from the right compartment equipped with a GC plate as WE, and an Ag/AgCl (3M KCl) as RE (filled with a 0.3 mM solution of 1-OH-AQ in 0.1 M NaOH).

2.4.4. Hydrogen peroxide quantification

Based on the spectroscopic method by Apaydin *et al.* [48] and Su *et al.* [76], UV-Vis measurements enabled the determination and quantification of H_2O_2 produced during electrolysis. Thereby, H_2O_2 reacts with 4-Nitrobenzeneboronic acid (p-NBBA) to the yellowish p-Nitrophenolate (p-NP) under basic conditions according to Scheme 3.
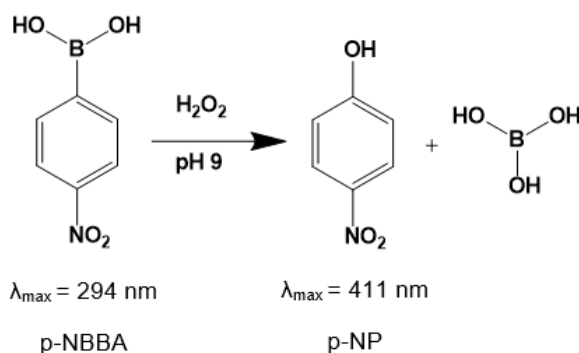
Scheme 3: Reaction scheme of p-NBBA to p-NP for the detection of H_2O_2.

Thus, a 4 mM p-NBBA solution in DMSO was prepared and mixed in a volume ratio of 1:1 with a 150 mM carbonate buffer with a pH value of 9. This mixture was then filtered through a syringe filter (pore size of 0.45 µm, RC). Furthermore, 50 µL of the 100 µL aliquots of the electrolyte solution as well as of a blank sample were transferred in small 4 mL brown vials. After adding 2 mL of the p-NBBA / carbonate buffer solution to each of the 50 µL electrolyte samples, the reaction proceeded for 36 min under dark conditions. Subsequently, three times 100 µL of each of those reaction mixtures were pipetted into microplates. All absorbance values of those samples were then simultaneously measured at 411 nm using a Thermo Scientific Multiscan GO Spectrometer. Moreover, for the quantification of H_2O_2 a calibration using H_2O_2 standard solutions was necessary. Hence, the determined absorbances of the standards with different concentrations were subtracted by the values of a blank sample. According to Figure 12, those Δabsorbance values can be plotted versus the wavelength and the calibration curve is obtained by using the Δabsorbance of the corresponding $n(H_2O_2)$ at 411 nm.
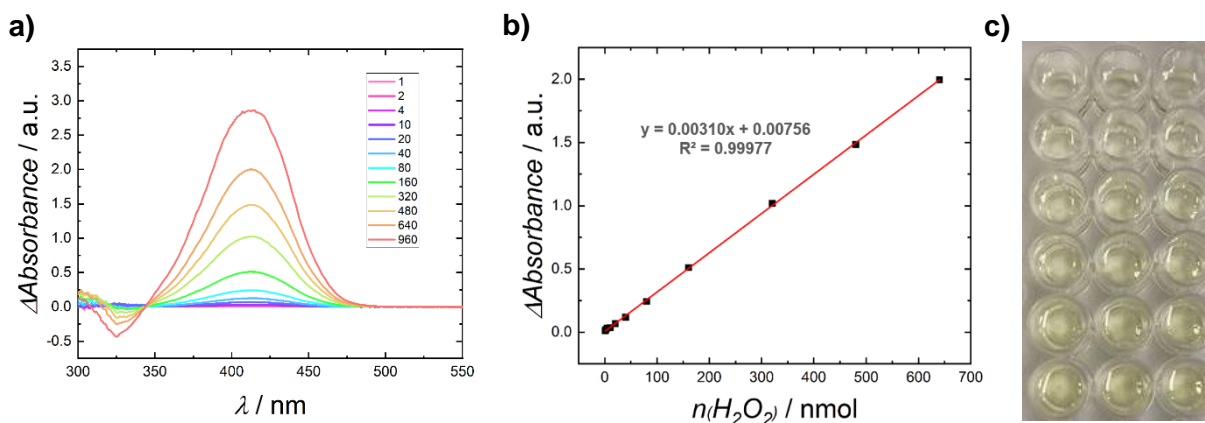
Figure 12: a) UV-Vis spectrum of the H_2O_2 calibration. b) Calibration curve using the Δabsorbance at 411 nm. c) Photograph of the detection plate during calibration.

Additionally, as the measured current over the electrolysis time (section 2.4.3.) is proportional to the charge (Q), the faradaic efficiency (FE) is calculated using Eq. 18 with the known $n_{product}$ [77].

$$FE(\%) = \frac{z_{reaction} \cdot n_{product} \cdot F}{Q} \cdot 100\% \qquad \text{(Eq. 18)}$$

F … faraday constant (96485 C mol^{-1})

Due to the two-electron reduction of oxygen, the value for $z_{reaction}$ is here 2.

2.5. UV-Vis spectroscopy

For the determination of the absorption maxima of the different AQ derivatives in 0.1 M NaOH as well as in pure MeCN, UV-Vis spectroscopical measurements were conducted. Thereby, a Varian Cary 3G UV-Visible Spectrophotometer was used (see chapter 2.2). The UV-Vis absorption spectra of the solutions in a quartz cuvette with a path length of 10 mm were recorded in a wavelength range of 250 to 800 nm. The appropriate concentration of the solutions was determined by diluting the dissolved compound until the absorbance range of the measurement was below 1. The resulting concentration of the materials in MeCN was 0.1 mM and the UV-Vis spectroscopic experiments in 0.1 M NaOH were conducted using either 0.025 mM or 0.05 mM solutions.

2.6. Fluorescence

The 1 mM solutions of the AQ derivatives in MeCN (0.6 mM ARS and 0.4 mM AQS) were also viewed under UV-light (λ=365 nm) in a dark room to identify their fluorescence.

3. Results and discussion

3.1. Spectroscopic comparison of different anthraquinone derivatives

3.1.1. UV-Vis spectroscopy in MeCN

For illustrative purposes, Figure 13 shows a photograph of various AQ derivatives dissolved in MeCN. The respective concentrations are 1 mM with the exceptions of a 0.6 mM ARS and a 0.4 mM AQS solution. The solutions are either colorless or yellowish.
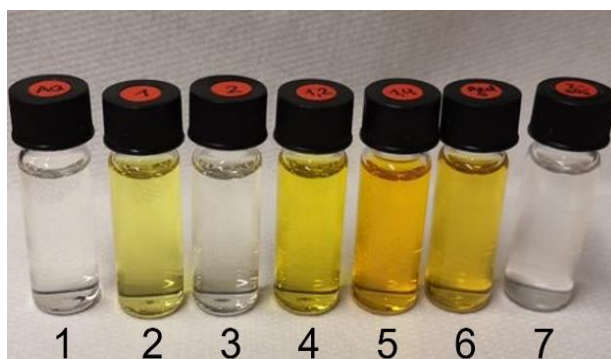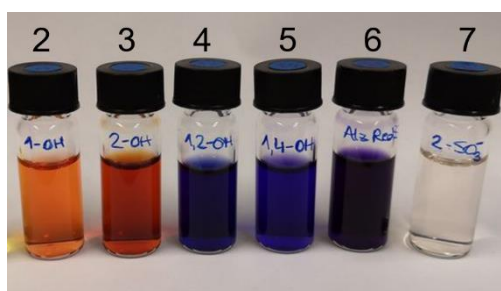

Figure 13: Demonstration of the different colors of the AQ compounds dissolved in MeCN, numbering in Table 4.

The exemplary UV-Vis absorbance spectra of the diluted solutions (0.1 mM) are displayed below, further spectra can be found in the appendix (Figure 43 and 44). Figure 14a demonstrates the spectrum of the unsubstituted AQ which is also representative for the sulfonated AQ. The 1-OH-AQ spectrum in Figure 14b is a representation for the monosubstituted AQ derivatives and the spectrum of 1,2-OH-AQ in Figure 14c resembles the one of 1,4-OH-AQ. The spectrum of the hydroxy-substituted as well as sulfonated AQ, ARS, is displayed in Figure 14d. All AQ derivatives show an absorption peak at around 325 nm and the hydroxy-substituted AQ`s have a second maximum. The corresponding peaks at the highest wavelength, the so-called absorption maxima, are listed in Table 4.
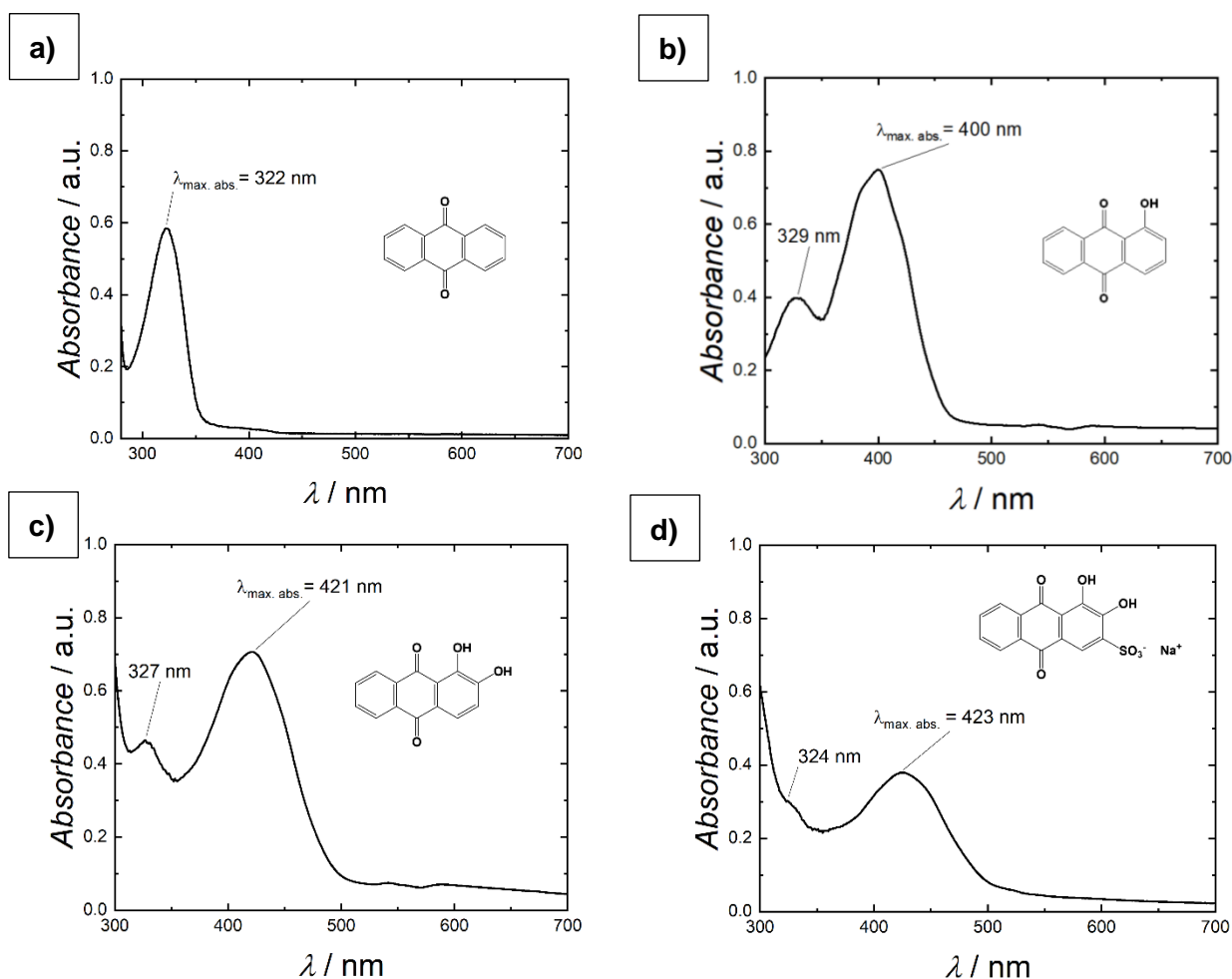
Figure 14: UV-Vis absorption spectra in MeCN with absorption maxima of a) AQ b) 1-OH-AQ c) 1,2-OH-AQ d) ARS.

Table 4: Absorption maxima of the 0.1 mM solutions of different AQ derivatives in MeCN, the numbers in brackets correspond to the solutions in Figure 13.

Substance	$\lambda_{max.\,abs.}$ / nm
AQ (1)	322
1-OH-AQ (2)	400
2-OH-AQ (3)	361
1,2-OH-AQ (4)	421
1,4-OH-AQ (5)	477
ARS (6)	423
AQS (7)	327

When comparing the absorption maxima with the colors of the solutions, it is obvious that the darker solutions have higher maxima values. The solutions with all maxima below 400 nm are colorless. These are AQ, 2-OH-AQ and AQS ($2\text{-}SO_3^-\text{-}AQ$) which indicates that the substitution at the position 2 has a lower impact on the absorbance. This is due to no or less hydrogen bonding between the substituents at position 2 and the carbonyl group [78]. Moreover, ARS has similar values as 1,2-OH-AQ and the only difference between those compounds is the additional sulfonate in the ARS. The maximum of AQS solution is also nearly the same as for the unsubstituted AQ. Thus, the sulfonate-group shows no important effect on the absorbance. Additionally, it can be seen that two hydroxy-groups shift the absorbance maximum to higher wavelengths compared to only one OH-group. The spectroscopic behavior of hydroxyanthraquinones depends on hydrogen bonds and the respective tautomers [79]. The determined maxima are in accordance with literature values [61,79].

3.1.2. UV-Vis spectroscopy in 0.1 M NaOH

In Figure 15, various 0.3 mM AQ derivative solutions in 0.1 M NaOH are shown to visualize the different color effects. Compared to the molecules in MeCN, the coloring of the compounds dissolved in NaOH are more pronounced and diverse. This is due to the resulting deprotonation of the hydroxyanthraquinones in alkaline solutions (pH = 13). While the dihydroxy-derivatives in NaOH show a violet-bluish color, the monohydroxy-AQs become red upon dissolution in NaOH. In contrast to this, AQS is colorless. The exemplary spectra of the 0.025 mM solutions (0.05 mM for AQS) are displayed in Figure 16 and further UV-Vis spectra are shown in the appendix (Figure 45 and 46). Furthermore, all determined absorption maxima are listed in Table 5.

Figure 15: Demonstration of the different colors of the AQ compounds dissolved in 0.1 M NaOH, numbering in Table 5.
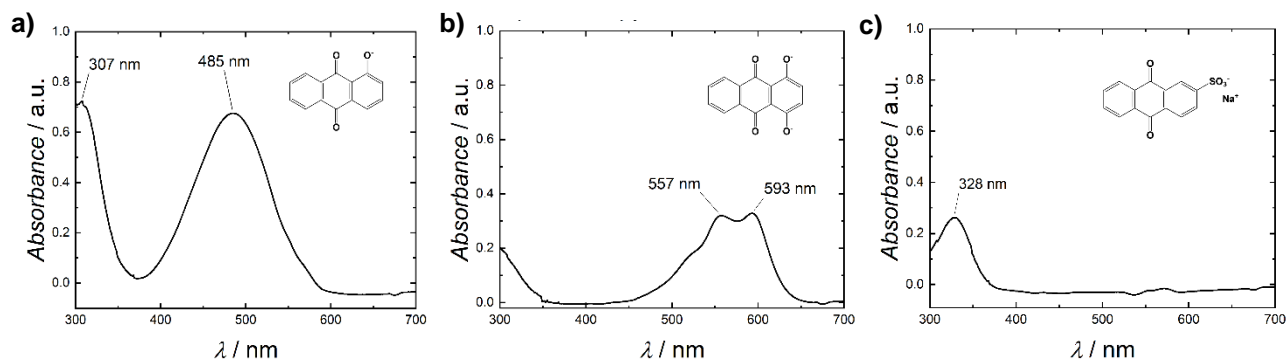
Figure 16: UV-Vis absorption spectra in 0.1 M NaOH with the absorption maxima of
a) 1-OH-AQ b) 1,4-OH-AQ and c) AQS.

Table 5: Absorption maxima of the solutions of different AQ derivatives in 0.1 M NaOH, the numbers in brackets
correspond to the solutions in Figure 15.

Substance	$\lambda_{max.\ abs.}$ / nm
1-OH-AQ (2)	485
2-OH-AQ (3)	467
1,2-OH-AQ (4)	568, 608
1,4-OH-AQ (5)	557, 593
ARS (6)	555, 595
AQS (7)	328

All AQ compounds in 0.1 M NaOH which were analyzed via UV-Vis spectroscopy can be categorized according to their absorbance maxima values. The red monohydroxylated AQ derivatives have peaks at around 300 nm and 480 nm, whereas the maxima of the violet dihydroxy-substituted AQs and ARS are found as twin-peaks at approximately 560 nm and 600 nm. Similar to the absorbance in MeCN (chapter 3.1.1.), it was expected that in 0.1 M NaOH ARS also behaves like 1,2-OH-AQ. However, the absorption maxima of ARS are nearly the same as the maxima of 1,4-OH-AQ. Despite the higher concentration, the less colored AQS still does not show high absorbance peaks. Although the only maximum of AQS at 328 nm is located at a higher wavelength than the 300 nm for the first peak of monohydroxy-AQs, AQS has in total the absorption maximum with the lowest energy. Additionally, it is obvious that the spectrum of AQS in 0.1 M NaOH is the same as in an aprotic organic solvent. Nevertheless, the UV-Vis spectroscopy of all other compounds yields different results in 0.1 NaOH than in MeCN. The difference in absorption maxima between the compounds in aqueous media compared to those in organic media (chapter 3.1.1.) can be explained by the deprotonation in pH 13 [80]. Due to the deprotonated form of the AQ derivatives in 0.1 M NaOH, a bathochromic shift is noticeable. As AQS has no hydroxy group to deprotonate, the absorption maximum remains constant. Thus, UV-Vis absorption is depending on not only the character and position of substituents but also on solvent effects, the protonation/deprotonation equilibrium and hydrogen bonds [79,80]. The same trend was recently reported by Schimanofsky [61].

Besides the study of the spectroscopic behavior, the purpose of performing UV-Vis spectroscopic experiments of the studied compounds in 0.1 M NaOH was to preclude the overlap of the absorption maxima with the applied wavelength (411 nm) for the H_2O_2 detection in chronoamperometric measurements (see chapter 2.4.4.).

3.1.3. Fluoresence in MeCN

The different fluorescent effects of various AQ compounds dissolved in MeCN (1 mM solutions) are displayed in Figure 17.
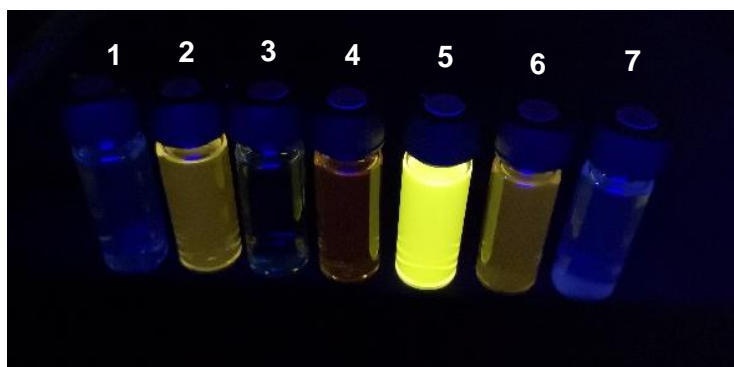
Figure 17: Fluorescent effects of 1mM solutions of different AQ derivatives in MeCN.
Numbering in the text below.

Figure 17 demonstrates that 1,4-OH-AQ (5) shows the highest fluorescence when excited with 365 nm, followed by the neglectable fluorescent effects of 1-OH-AQ (2), 1,2-OH-AQ (4) and ARS (6). AQ (1), 2-OH-AQ (3) and AQS (7) are not fluorescent at all. This leads to the assumption that derivatives with substitutions at positions 1 and 4, like 1,4-OH-AQ and 1-OH-AQ, are more influenced than the AQ compounds with functional groups at different positions. In addition, the excitation wavelength of 365 nm seems to be too high for AQ, 2-OH-AQ and AQS to fluoresce.

3.1.4. Decay of 1,4-OH-AQ

Upon the storage of 1,4-OH-AQ solutions in 0.1 M NaOH in closed vials (Figure 18), a disappearance of the dark violet color was observed. After 2 months the before violet colored solution became completely transparent and colorless.
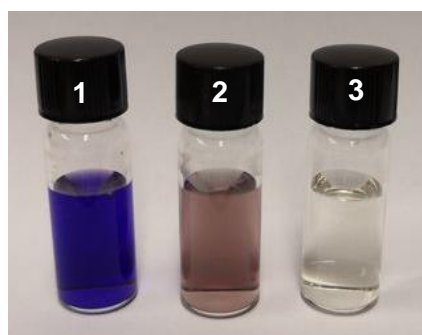
Figure 18: Color disappearance of different 1,4-OH-AQ solutions in 0.1 M NaOH over time: 1) freshly made 0.3 mM solution, 2) 1 mM solution after 1 week of storage 3) 1.5 mM solution after 2 months of storage.

In addition, delta absorbance spectra of various samples of 0.3 mM 1,4-OH-AQ in 0.1 M NaOH were recorded during a chronoamperometry under O_2 (chapter 2.4.3. and 3.5.). These samples were taken at 0 h, 1 h, 2 h, 4 h and 6 h and showed a color loss. Those spectra, depicted in

Figure 19, show not only the H_2O_2 detection peak at 413 nm which is increasing over electrolysis time, but also a broad decreasing peak corresponding to 1,4-OH-AQ. This peak consisting of small maxima at 557 nm and 592 nm is in agreement with the absorption maxima of 1,4-OH-AQ (557 nm and 593 nm) shown in Figure 16 and Table 5.
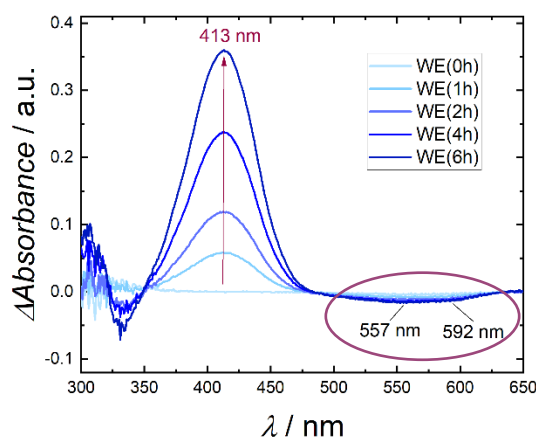
Figure 19: UV-Vis spectra of the electrolysis samples of 0.3 mM 1,4-OH-AQ solution in 0.1 M NaOH at different times.

Due to these findings, a further UV-Vis spectroscopy study was conducted to monitor the decay of 1,4-OH-AQ. Thereby, a 0.5 mM solution of 1,4-OH-AQ in 0.1 M NaOH was prepared and stored in an unclosed vial allowing a constant contact with air. Every few hours within a period of 8 days a spectrum of a sample of this solution was recorded. In Figure 20a, those spectra are depicted and show again the characteristic peaks at 558 nm and 594 nm which are decreasing over time. Moreover, the UV-Vis absorbance measurements at the wavelengths of the absorption maxima (558 nm and 594 nm) enable the plot of the delta absorbance as a function of time (Figure 20b). In Figure 20b an exponential-like decrease in delta absorbance over time is shown. This decrease is accompanied by a visible color gradient of the 1,4-OH-AQ solution with increasing time.
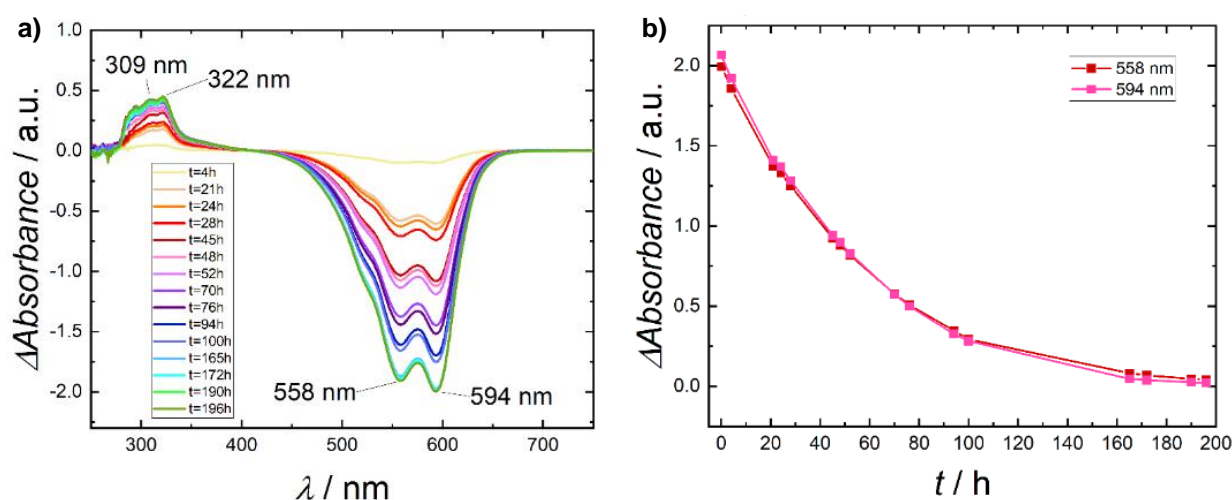
Figure 20: Decay of 0.5 mM 1,4-OH-AQ in 0.1 M NaOH: a) ΔAbsorbance after time as a function of wavelength. b) ΔAbsorbance at 558 nm and 594 nm against time.

The degradation and decolorization of 1,4-OH-AQ was already reported by Itoh *et al.* where the so-called Pigment Violet 12 was biologically degraded into phthalic acid and benzoic acid using a

fungus [81]. Similar microbial biodegradation processes of anthraquonine dyes have been published [82–85]. However, the explanation and mechanism of the aerobic decolorization in 0.1 M NaOH is not yet fully understood. Thus, further research work would be necessary.

3.2. Cyclic voltammetry in MeCN

As already stated in chapter 2.4.1., CV measurements in organic media (0.1 M TBAPF$_6$ in MeCN) were performed using 1 mM solutions of various AQ derivatives for a first electrochemical characterization. The only exception was the less soluble AQS solution in MeCN with a concentration of 0.5 mM. The respective CV graphs at 200 mV s^{-1} with the reduction and re-oxidation peaks are summarized in Figure 21. This two one-electron step mechanism of the reduction of AQs in aprotic solvents is in accordance to literature [61,86].
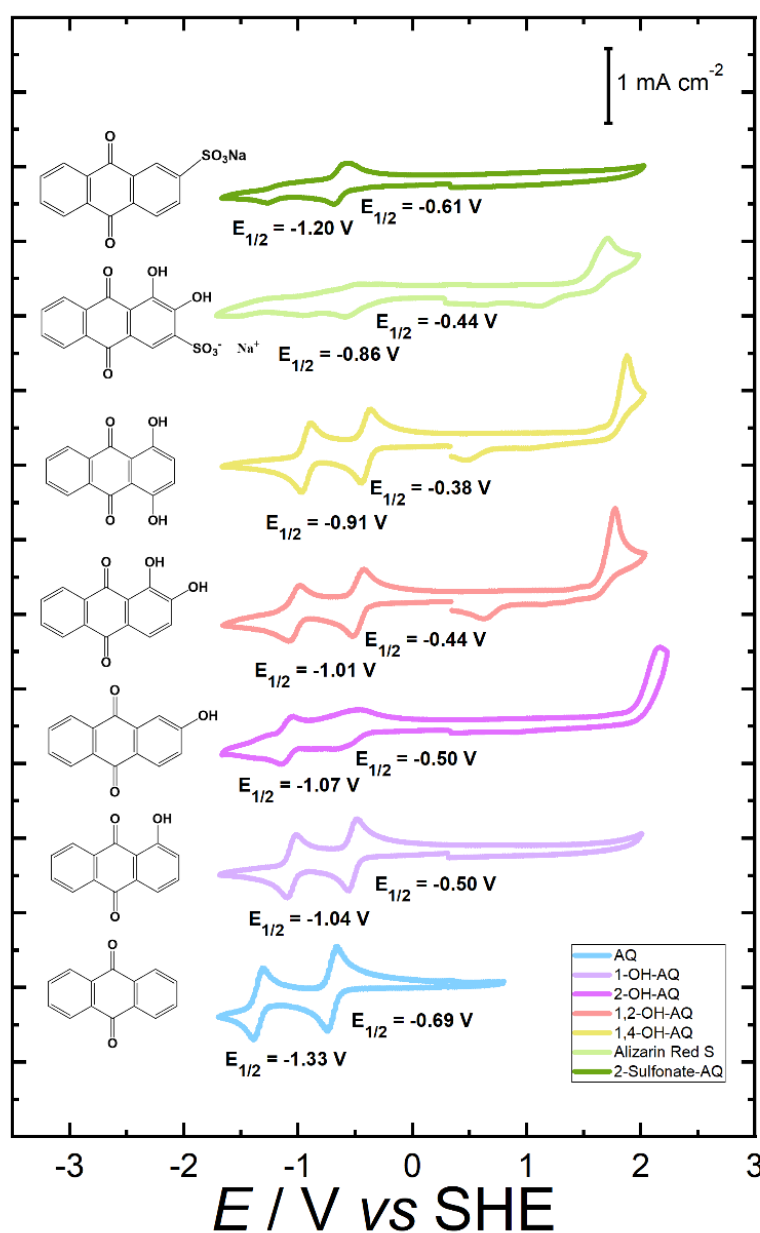
Figure 21: CV graphs of different AQ derivatives in MeCN at 200 mV s^{-1}.

Some compounds show an oxidation peak in the measured range (at 1.5-2 V vs SHE). While the oxidation of the monohydroxy-anthraquinone is irreversible, the curves of 1,2-OH-AQ, 1,4-OH-AQ and ARS also show a small re-reduction peak. As AQ, 1-OH-AQ and AQS oxidize at higher potentials, the used potential range was not sufficiently anodic to detect the respective oxidations. Similar results concerning the shape of graphs, reversibility and potentials were obtained by Schimanofsky [61]. Nevertheless, this further oxidation destroys the system and prevents the reproducibility of this graph afterwards. However, the determination of those peaks becomes essential when finding a suitable ring potential for RRDE measurements (chapter 3.4.1.).

For each reduction peak a so-called half-wave potential ($E_{1/2}$) was determined. The unsubstituted AQ has the most cathodic reduction half-wave potentials, followed by AQS which also shows less pronounced peaks. Due to well discernible redox peaks and an additional oxidation peak, the curves for 1,2-OH-AQ and 1,4-OH-AQ look very similar, besides the fact that the half-wave potentials of the 1,4-OH-AQ are shifted towards more positive potentials. Furthermore, 1-OH-AQ and 2-OH-AQ resemble each other with regard to the $E_{1/2}$-values but a lower anodic shift than for the dihydoxylated AQs is observable. ARS has the least defined peaks and behaves like a mixture of the two dihydroxy-substituted AQs. The first reduction peak is in compliance with the peak of 1,2-OH-AQ and the second reduction step resembles the one of 1,4-OH-AQ. In comparison to the unsubstituted AQ, all investigated derivatives reduce at more anodic potentials, especially hydroxylated compounds. This can be explained by the formation of hydrogen bonds between the OH-substituent and the adjacent carbonyl group stabilizing the radical intermediate [78]. Additionally, substitutions on the position 1 (or 4) increase the reduction tendency by increasing the hydrogen bonding [78]. This results in more positive potential shifts than substituting the hydrogen on position 2 where intramolecular hydrogen bonds are less favored. Similar results and substitution effects were also reported in literature [61,86,87]. The dependence of the redox potentials of AQ molecules on the position as well as nature of the functional groups stems from the different inductive and resonance effects of the substituents [78,86]. Although OH-groups are electron-withdrawing regarding the electronegativity of oxygen, the mesomeric effect leads to electron-donation [87]. On the other hand, sulfonate acts as an inductive electron-withdrawing group [88].

3.3. Cyclic voltammetry in aqueous media

3.3.1. CV measurements in pH 13

The CV graphs of various 1 mM AQ-derivative solutions (0.4 mM 1-OH-AQ) in pH 13 using a scanrate of 200 mV s^{-1} are compared to the blank CV under O_2 using pure 0.1 M NaOH. Some exemplary comparisons are displayed in Figure 22 and further graphs can be found in the appendix (Figure 47 and 48). The peak of the blank measurement corresponds to the O_2 reduction on GC, the CV under N_2 shows the AQ reduction and both the O_2 as well as AQ reduction were observed in the CV of the AQ solution under O_2 environment. In Table 6, the determined half-wave potentials for the reductions and the onset potentials for further oxidation peaks can be seen. While the curve under N_2 shows the AQ reduction and the blank GC reduces only O_2, the CV graph using the respective AQ under O_2 conditions is composed of a mixture of the AQ and O_2 reduction.
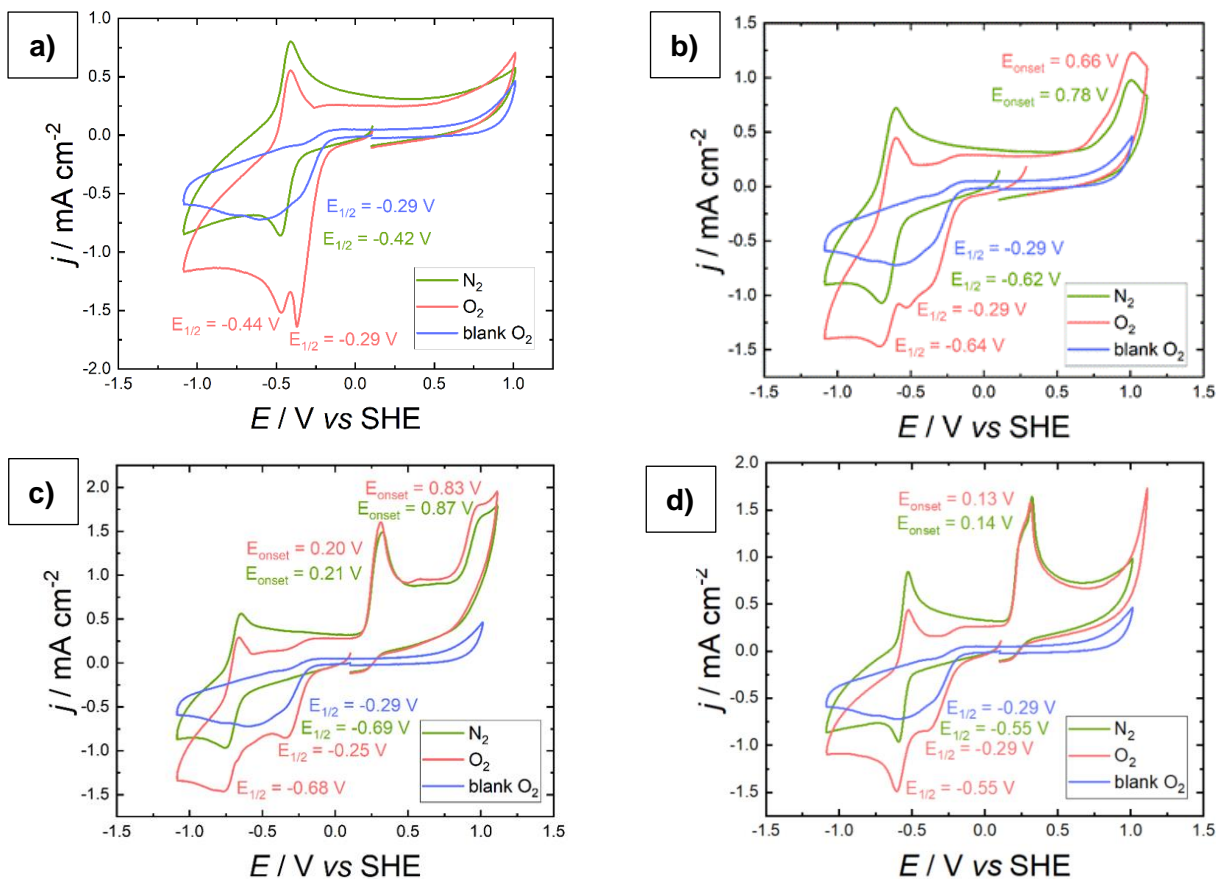
Figure 22: CV graphs of 1 mM solution in 0.1 M NaOH at 200 mV s^{-1} of a) AQS b) 2-OH-AQ
c) 1,2-OH-AQ d) 1,4-OH-AQ.

Table 6: Reduction and oxidation peaks of different 1 mM AQ derivatives in 0.1 M NaOH (exception: 0.4 mM 1-OH-AQ solution in NaOH).

Compound	$E_{1/2,reduction}$ / V vs SHE		$E_{onset,oxidation}$ / V vs SHE	
	N$_2$	O$_2$	N$_2$	O$_2$
Blank GC	-	-0.29	-	-
AQS	-0.42	-0.29 and -0.44	-	-
2-OH-AQ	-0.62	-0.29 and -0.64	0.78	0.66
1-OH-AQ	-0.54	-0.26 and -0.52	0.58	0.50
1,2-OH-AQ	-0.69	-0.25 and -0.68	0.21 and 0.87	0.20 and 0.83
1,4-OH-AQ	-0.55	-0.29 and -0.55	0.14	0.13
ARS	-0.70	-0.29 and -0.73	0.29	0.29

When comparing the E$_{1/2}$-values, it might be assumed that only 1-OH-AQ and 1,2-OH-AQ enhance the O$_2$ reduction by shifting the reduction to more positive potentials. The location of the half-wave potentials for the O$_2$ reduction of the other AQ derivatives does not differ from the -0.29 V vs SHE for blank GC. Additionally, the reduction half-wave potentials for the AQ peaks remain nearly

constant when changing the gas environment from N_2 to O_2. However, all studied compounds increase the reductive current (density) between -0.15 V and -1.1 V vs SHE which is the range where both the O_2 and AQ reductions occur. As seen in Figure 22, these O_2 reductions also have a slightly earlier onset potential compared to blank GC.

Furthermore, the conduct of RRDE experiments demands the determination of an appropriate ring potential. The oxidations of the AQ derivatives narrow the possible range because the applied ring potential must be more negative than these. Thus, the onset potentials of those oxidations were determined. As seen in Table 6, the dihydroxy-AQs oxidize at moderately positive potentials which hinders the application of a suitable ring potential for 1,2-OH-AQ and 1,4-OH-AQ (compare Figure 25a). In addition, there was no oxidation of AQS observed in the measured potential range and the onset potentials of the monohydroxylated AQ compounds are much more positive than the onset of ARS (Table 6). Consequently, the oxidation of ARS is the upper limit for the ring potential that is used for all compounds (except 1,2-OH-AQ and 1,4-OH-AQ). In chapter 3.4.1, more detailed information regarding the ring potential is mentioned.

3.3.2. CV measurements in pH 7 and pH 2

Due to the decreased proton dissociation in neutral media, a lower solubility of hydroxylated AQs in phosphate buffer (PB) was observed. Therefore, only CVs of ARS and AQS were recorded. When comparing the CV in pH 7, shown in Figure 23, with the CV graphs in pH 13 (chapter 3.3.1. and Figure 22), a pH effect is observable. The lower the pH, the more positive gets the potential of the reduction and oxidation [89]. The dependence on the pH can be explained by the reaction according to Eq. 16 and Eq. 17 where H^+ ions play a major role. Contrary to the expectations, the O_2 reduction of the blank GC changes as to more negative potentials from pH 13 to pH 7 and remains at the same position when decreasing the pH to a value of 2 (Figure 24).
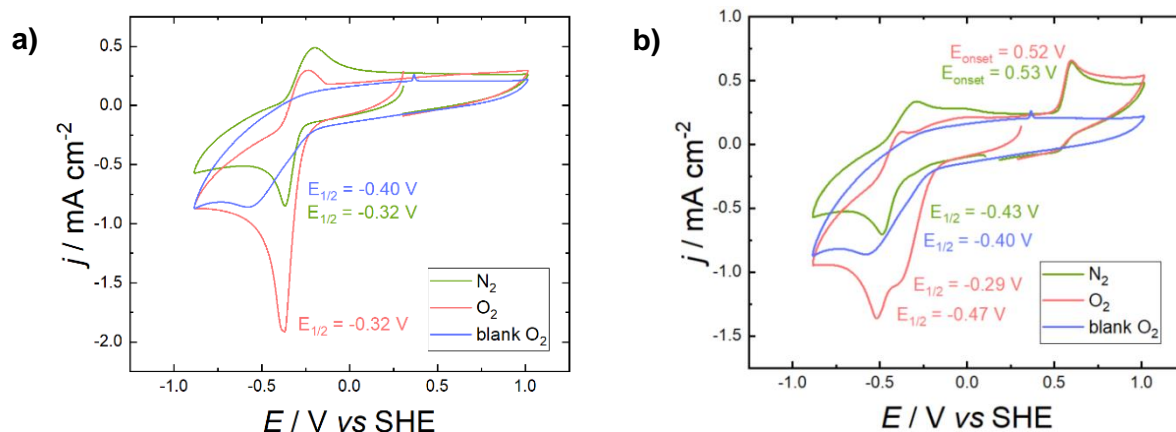
Figure 23: a) CV of 1 mM AQS in PB with pH 7 at 200 mV s^{-1}. b) CV of 1 mM ARS in PB with pH 7 at 200 mV s^{-1}.
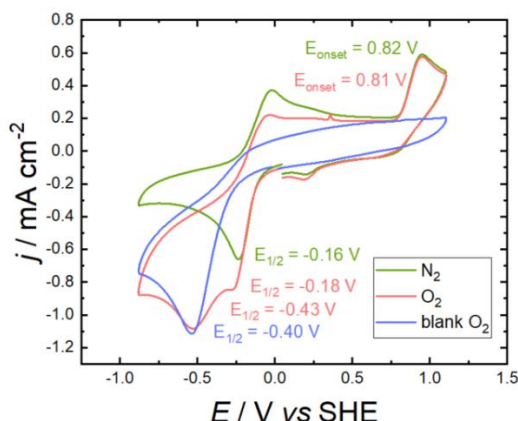
Figure 24: CV of 1 mM ARS in PB with pH 2 at 200 mV s^{-1}.

Since a separate reduction peak of O_2 is missing in the AQS curve in pH 7 under O_2 (Figure 23a), an overlap of both reductions can be assumed. For a better understanding of the pH impact, the determined half-wave potentials at different pH values are listed in Table 7.

Table 7: Determined half-wave potentials at different pH values.

Compound	$E_{1/2,N_2}$ / V vs SHE			$E_{1/2,O_2}$ / V vs SHE		
	pH 13	pH 7	pH 2	pH 13	pH 7	pH 2
Blank GC	-	-	-	-0.29	-0.40	-0.40
AQS	-0.42	-0.32	-	-0.29, -0.44	-0.32	-
ARS	-0.70	-0.43	-0.16	-0.29, -0.73	-0.29, -0.47	-0.18, -0.43

When comparing the ARS solution in pH 2 (Figure 24) with pH 7 and 13, a shift of the anodic and cathodic peaks to more positive potentials is observable. However, the first reduction peak of ARS in pH 7 under O_2 (Figure 23b) has the same half-wave potential as in pH 13. In pH 7 and 13 the onset of the ARS reduction is anodically shifted and the respective reduction currents are more negative. In contrast to this, in pH 2 the reductive current is increased without changing the onset. Moreover, the O_2 reduction current using ARS in pH 2 is even lower than for blank GC. Nevertheless, the increased current of the AQ reduction in O_2 compared to N_2 condition indicates a low catalytic activity of ARS in pH 2. Besides the already mentioned exception for the blank GC, the AQ compounds show a shift to more positive potentials with decrease in pH.

3.4. Comparison of different anthraquinone derivatives based on the RRDE method

After the observations via the CV measurements, the rotating ring-disc (RRDE) method was used for further investigations of the electrocatalytic activity of different AQ derivatives regarding the reduction of O_2 to H_2O_2.

3.4.1. Preparatory work for RRDE method

The possible potential that can be applied at the ring has to be determined to be able to perform RRDE measurements. Therefore, using the RRDE CV graphs of GC and Pt in 0.1 M NaOH under O_2 and N_2 conditions were recorded. Similarly, CV was performed in 0.1 M NaOH with 5 mM H_2O_2 (see Figure 25a). Thereby, the half-wave potentials for the H_2O_2 reduction as well as oxidation and the $E_{1/2}$-value for the ORR can be determined.
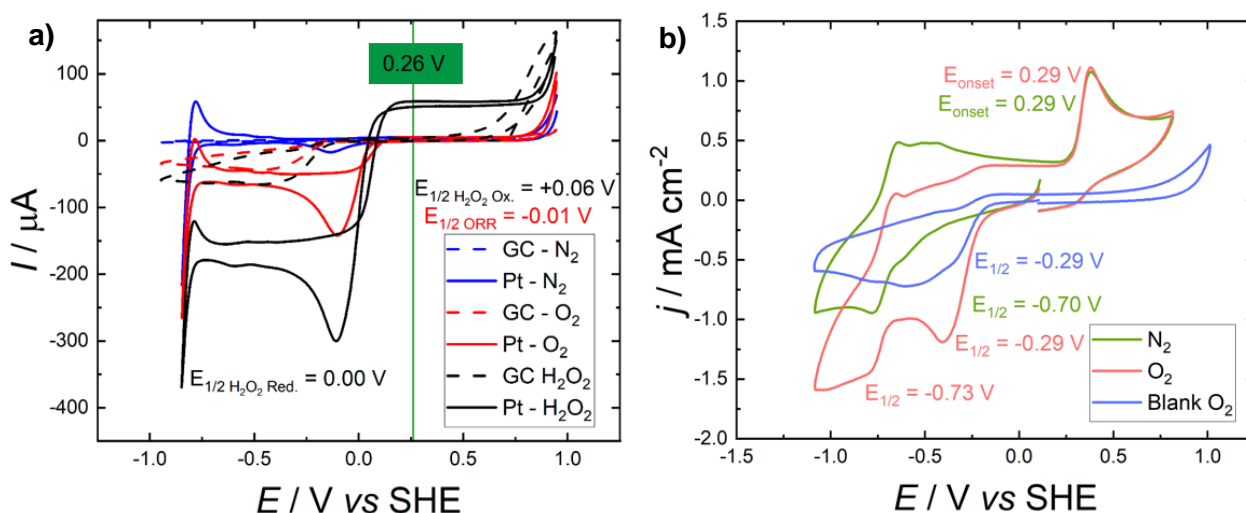
Figure 25: CV graphs for the determination of the ring potential: a) CVs with $E_{1/2}$ values for the H_2O_2 reduction and oxidation as well as for the oxygen reduction. b) CV of 1 mM ARS in 0.1M NaOH with the determined E_{onset} of its oxidation.

By addition of H_2O_2 the potential remains unchanged while the reductive current is increased. The target of the study of the ORR via the RRDE method is the detection of H_2O_2 that is formed at the disc via re-oxidation at the ring. As a result, the applied potential at the ring has the requirement to be more positive than +0.06 V vs SHE. However, the oxidation of the different AQ compounds (like the oxidation of ARS in Figure 25b) limits the potential range from the other side. As seen in Table 6, the oxidation onset potentials of 1,2-OH-AQ and 1,4-OH-AQ are not sufficiently high/positive to avoid kinetic limitations. Therefore, a complete RRDE study of those compounds is not possible. In order to ensure the same conditions for all other molecules, the next lowest oxidation onset potential (+0.29 V vs SHE for AQS) is used as upper limit. Thus, a constant ring potential of +0.26 V vs SHE was chosen.

For calibrating the RRDE system, RRDE measurements with $K_3[Fe(CN)_6]$ in 0.1 M NaOH were performed (Figure 26). Consequently, the collection efficiency N which is a significant parameter for quantitative RRDE experiments can be determined according to Eq. 12 using this Fe^{3+}/Fe^{2+} redox couple. Due to the relation of the mass transport rate to the rotational speed, faster rotation of the electrode leads to an increase of the rate of material arriving at the surface of the electrode. Therefore, the absolute limiting current is higher for faster rotation rates. This dependence on the speed can be seen in Figure 26.
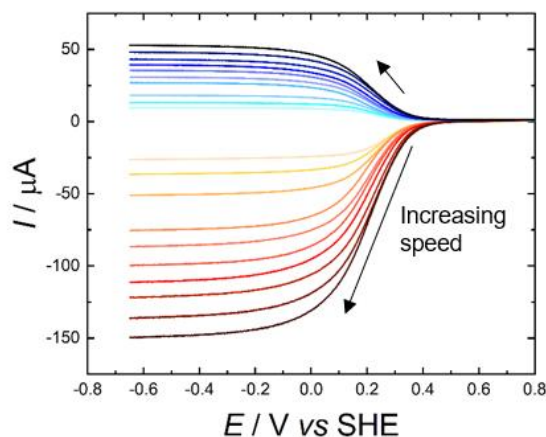
Figure 26: LSV of K$_3$[Fe(CN)$_6$] in 0.1 M NaOH using different rotational speeds under N$_2$ conditions. Red curves correspond to the disc and blue curves to the ring.
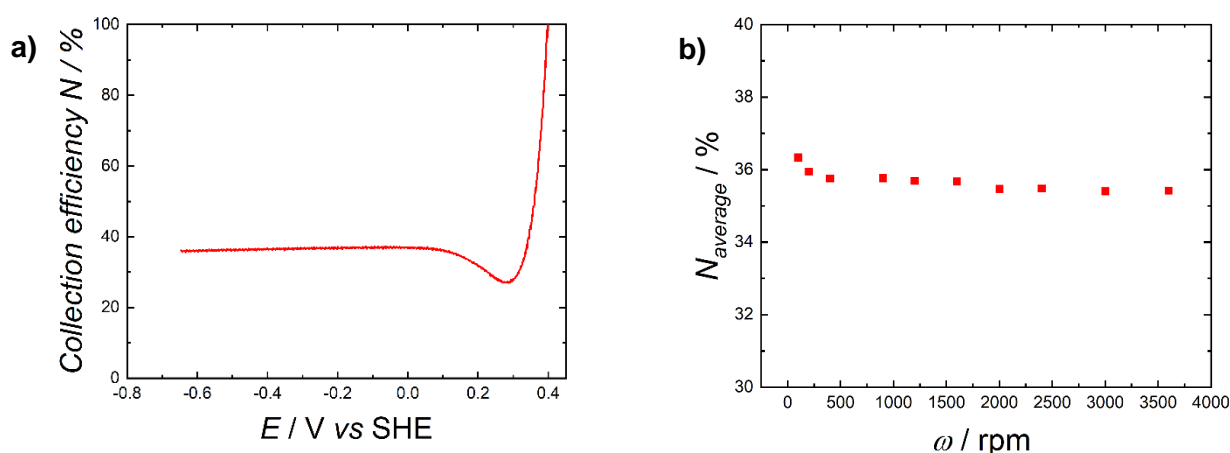
Figure 27: a) Experimental collection efficiency N for 100 rpm plotted against the respective potential. b) Average collection efficiencies at the corresponding rotation rates.

As can be seen in Figure 27a, the calculated efficiency N remains nearly constant between -0.3 V and -0.65 V. Hence, for each rotation rate the N-values in this range can be averaged and those summarized efficiencies can be plotted against the respective speeds (Figure 27b). The thereby determined $N_{average}$ values range between 35 % and 36 %. Those averaged collection efficiencies corresponding to different rotational speeds were used for further calculations.

3.4.2. RRDE method in pH 13

After the determination of a suitable ring potential, the calibration of the RE and the calculation of each $N_{average}$, the electrocatalytic behavior of the different AQ derivatives regarding the O$_2$ reduction towards H$_2$O$_2$ can be characterized using the RRDE method. The recorded LSV graphs of the 0.4 mM solutions of the AQ compounds in 0.1 M NaOH with pH 13 at 900 rpm can be plotted to compare N$_2$ saturated conditions and O$_2$ saturated conditions with the blank O$_2$ measurement in 0.1 M NaOH. As the AQ-O$_2$ system seems to be composed of both the GC-O$_2$ and AQ-N$_2$ system, the so-called electrocatalytic excess current can be determined using the following formula established by Wielend *et al.* [45]:

$$I_{excess} = I_{AQ,O_2} - (I_{GC,O_2} + I_{AQ,N_2})$$
(Eq. 19)

This mathematical approach was applied to the currents at the disc as well as to the ring currents at each rotation speed. The graphical depiction of those excess currents reveals the catalytic

range of a substance. In addition, the respective efficiencies at every rotation rate can be calculated via Eq. 14 with the use of the excess currents at the ring and at the disc. The three graphical illustrations mentioned above are displayed below for all AQ derivatives. However, the ring excess currents of the dihydroxy-AQs cannot be determined because of the low oxidation onset potentials (see Table 6). Hence, a different constant ring potential (+0.05 V vs SHE) was applied for N_2 conditions and in the O_2 environment only the disc currents were recorded. The missing data hinders the determination of the efficiency plots for 1,2-OH-AQ and 1,4-OH-AQ.
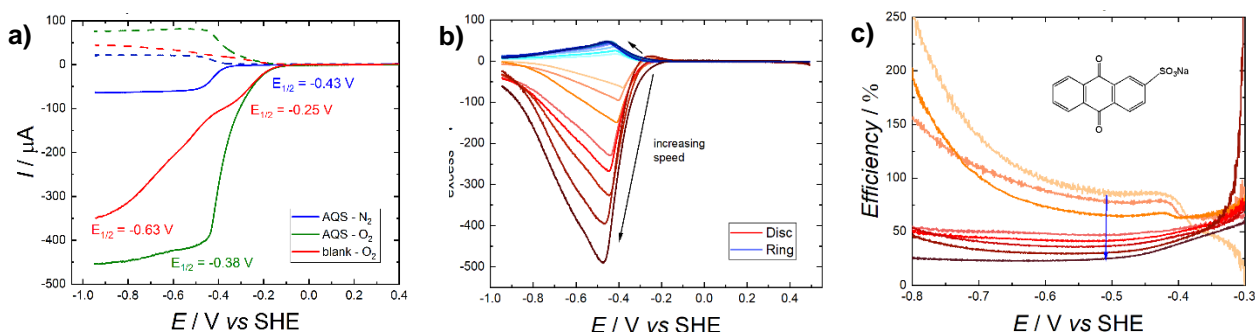
Figure 28: LSV at 900 rpm of 0.4 mM AQS in 0.1 M NaOH in O_2/N_2 environment compared to blank O_2 LSV at 900 rpm. b) Excess currents at the ring and disc at several rotation rates plotted against the potential. c) Resulting efficiencies at the different rotational speeds as functions of the potential.
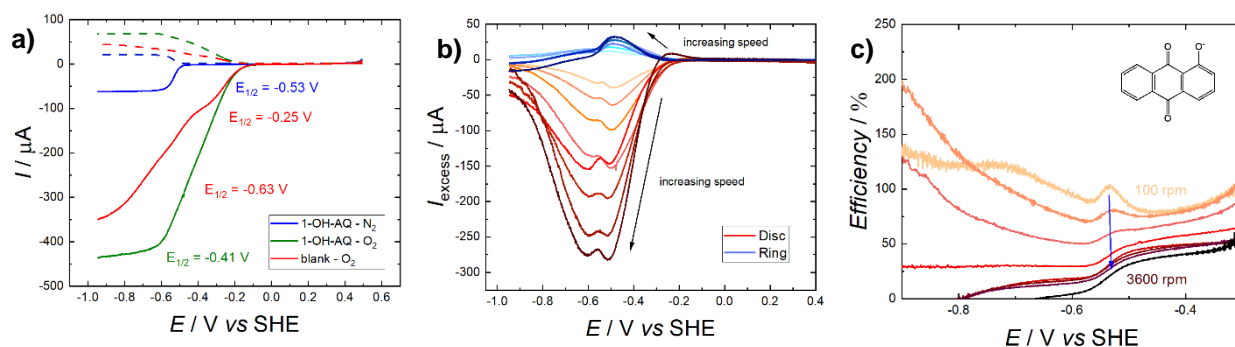
Figure 29: a) LSV at 900 rpm of 0.4 mM 1-OH-AQ in 0.1 M NaOH in O_2/N_2 environment compared to blank O_2 LSV at 900 rpm. b) Excess currents at the ring and disc at several rotation rates plotted against the potential. c) Resulting efficiencies at the different rotational speeds as functions of the potential.
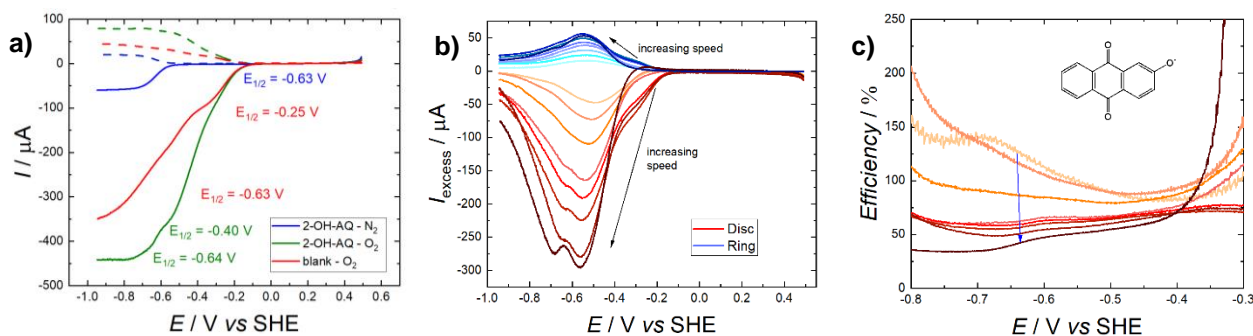
Figure 30: a) LSV at 900 rpm of 0.4 mM 2-OH-AQ in 0.1 M NaOH in O_2/N_2 environment compared to blank O_2 LSV at 900 rpm. b) Excess currents at the ring and disc at several rotation rates plotted against the potential. c) Resulting efficiencies at the different rotational speeds as functions of the potential.
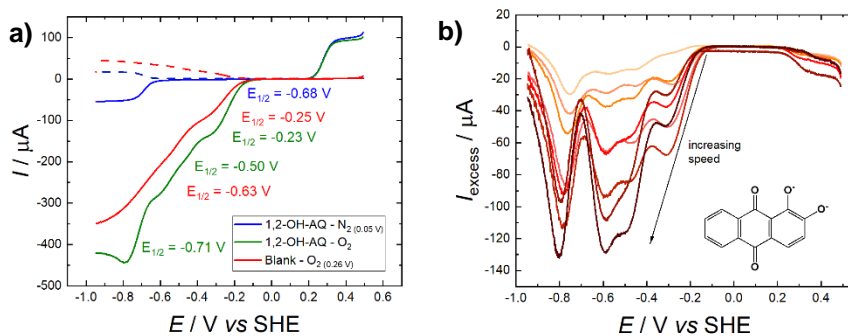
Figure 31: a) LSV at 900 rpm of 0.4 mM 1,2-OH-AQ in 0.1 M NaOH in O_2/N_2 environment compared to blank O_2 LSV at 900 rpm. b) Excess currents at the disc at several rotation rates plotted against the potential.
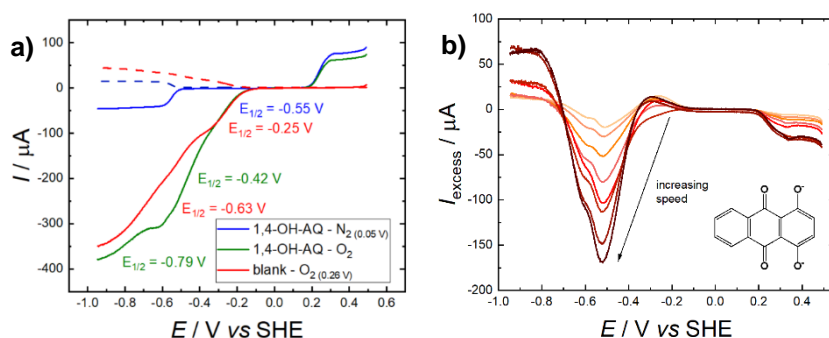
Figure 32: a) LSV at 900 rpm of 0.4 mM 1,4-OH-AQ in 0.1 M NaOH in O_2/N_2 environment compared to blank O_2 LSV at 900 rpm. b) Excess currents at the disc at several rotation rates plotted against the potential.
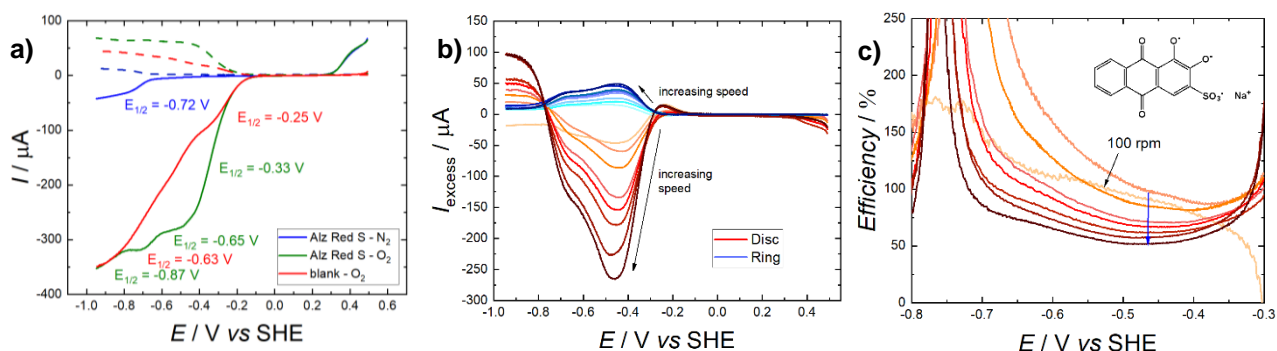
Figure 33: a) LSV at 900 rpm of 0.4 mM ARS in 0.1 M NaOH in O_2/N_2 environment compared to blank O_2 LSV at 900 rpm. b) Excess currents at the ring and disc at several rotation rates plotted against the potential. c) Resulting efficiencies at the different rotational speeds as functions of the potential.

All LSV curves in N_2 saturated conditions behave nearly ideally which is expressed by a stable mass transport limited region at a certain potential and by the steep step of the reductive current. Nevertheless, some molecules show a steeper step than others and according to the different half-wave potentials also the mass-transport regime varies between the different compounds, but it is observable at around -0.7 V vs SHE. The plots of the excess currents show the catalytic regions of each AQ where the current values of the AQ-O_2 system exceed the linear combination of both components. After the peak(s) with high negative excess currents, the excess current curve moves again towards zero. Additionally, for faster rotation rates an increase of excess currents is observable. Except ARS, all other AQ molecules with efficiency plots show at 100 rpm a little peak at certain potentials. For a better comparison of the catalytic effects of the substances, to identify a trend and to attempt at quantification, some data was determined and summarized in Table 8 as well as depicted in Figure 34. These are the highest excess currents ($I_{excess,max}$), the potentials at those maxima ($E(I_{excess,max})$), the onset potentials of the catalytic regions of the excess current and the potentials at the efficiency peaks.

Table 8: Summary of the determined maxima of the excess currents ($I_{excess,max}$) with the corresponding potentials ($E(I_{excess,max})$), the onset potentials of the catalytic regions ($E_{onset}(I_{excess})$) and the potentials at the efficiency maxima ($E(Efficiency_{max})$).

Substance	$I_{excess,max}$ / μA	$E(I_{excess,max})$ / V vs SHE	$E_{onset}(I_{excess})$ / V vs SHE	$E(Efficiency_{max})$ / V vs SHE
AQS	-491	-0.47	-0.31	-0.42
1-OH-AQ	-283 and -277	-0.51 and -0.60	-0.31	-0.53
2-OH-AQ	-296 and -275	-0.56 and -0.69	-0.34	-0.69
1,2-OH-AQ	-129 and -132	-0.59 and -0.81	-0.17	-
1,4-OH-AQ	-169	-0.52	-0.37	-
ARS	-265	-0.47	-0.30	-
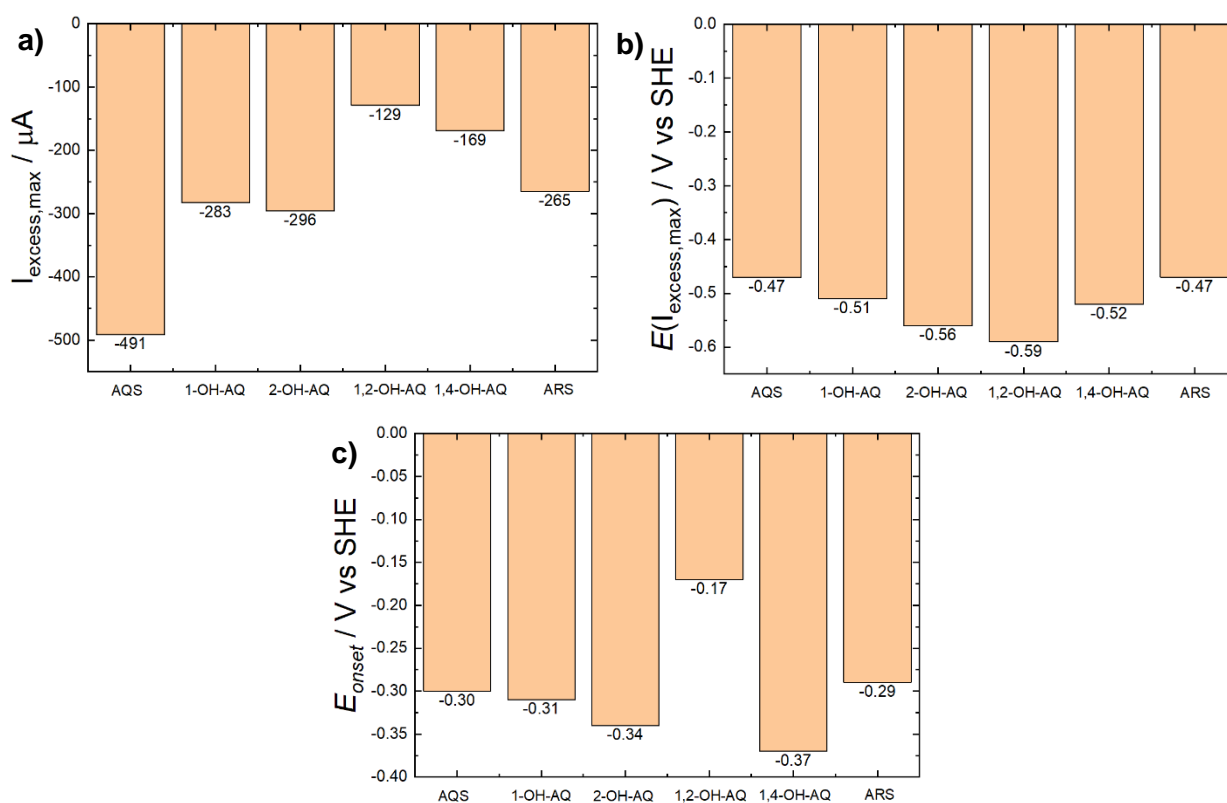
Figure 34: Visual comparison of a) maxima of the excess currents ($I_{excess,max}$) with b) the corresponding potentials ($E(I_{excess,max})$) and c) the onset potentials of the catalytic regions ($E_{onset}(I_{excess})$).

In spite of the considerable high maximal excess current of AQS, only one peak is visible in Figure 28b. In comparison to this, 1-OH-AQ, 2-OH-AQ and 1,2-OH-AQ show more than one peak yielding a broader range with high excess currents. Hence, not only the value of $I_{excess,max}$ is relevant, but also the number of maxima. In addition, Figure 34a demonstrates that the monohydroxylated AQs have higher excess currents than the dihydroxyanthraquinones. On the one hand, it is noticeable that AQ derivatives with a substitution at position 2, namely AQS, 2-OH-AQ and ARS, have high maxima of excess currents. Although 1,2-OH-AQ has two peaks, the excess current maximum is exceptionally low. On the other hand, the potentials at the maxima

(Figure 34b) demonstrate that derivatives with a hydroxy-group at the position 2 (2-OH-AQ and 1,2-OH-AQ) have the most negative potentials at the maxima but sulfonated anthraquinones with substitutions at position 2 have the most positive potentials. The potential values at the maximal excess currents suggest no relevant trend regarding the number of hydroxy-groups. While the excess current seems to be dependent on the number of the functional group, the potential at the maxima is more influenced by the position of the substitution. Despite the low maximal excess current of 1,2-OH-AQ, this substance has a significant low onset potential, a high potential at the maximum as well as several peaks in the excess current plot. This results in a very broad catalytic region with high excess currents. The sulfonated AQ compounds show also highly positive onset potentials of the catalytic range (Figure 34c), followed by the monohydroxy-substituted AQ molecules. Contrary to 1,2-OH-AQ, the catalytic excess current range of 1,4-OH-AQ starts at a highly negative potential. The comparison of the parameters for the electrocatalytic behavior for the O_2 reduction reveals that AQS has by far the highest maximal excess current at the most positive potential, one of the lowest onset potentials and a good efficiency. In contrast to this, 1,4-OH-AQ proves to have overall the lowest catalytic activity, followed by 1,2-OH-AQ which, however, has an exceptional low onset potential. Nevertheless, a complete RRDE study of dihydroxylated AQs with the application of a ring potential was impossible. The catalytic effects of 1-OH-AQ, 2-OH-AQ and ARS for the H_2O_2 production through RRDE experiments seem to lie in between.

3.4.3. RRDE method in pH 7 and pH 2

The RRDE experiments were also performed in pH 7. However, only ARS and AQS were sufficiently soluble in PB. The determination of the ring potential was conducted similarly as in pH 13. The resulting CV graphs are displayed in Figure 35a and reveal that the ring potential must be more positive than +0.44 V vs SHE. This finding is in accordance to literature [45].
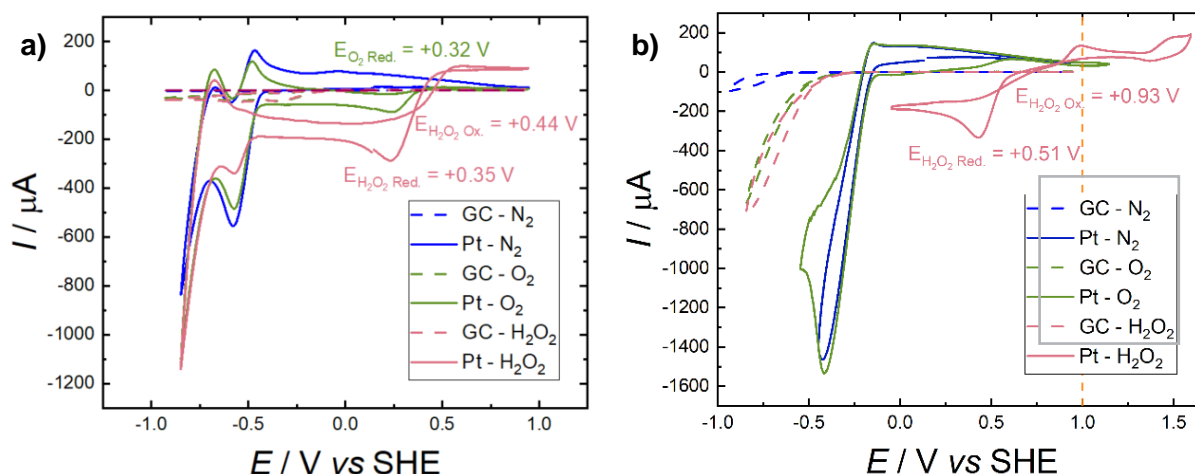
Figure 35: Comparison of CV graphs of Pt and GC electrodes under N_2, O_2 or in 5 mM H_2O_2
a) in PB with pH 7 b) in PB with pH 2.

Furthermore, as shown in Figure 23, the oxidation of ARS in pH 7 with an onset potential of +0.52 V vs SHE would limit the possible range of potentials too much. Therefore, RRDE experiments in pH 7 with a constant ring potential of +0.60 V were only performed using AQS. The ARS solution in pH 7 was measured using a ring potential of +0.50 V vs SHE which only allows the determination of the disc excess currents. In Figure 36, the LSV curves of ARS and AQS in pH 7 are displayed. RRDE measurements in PB with pH 2 were not conducted but according to

Figure 35b a ring potential higher than +1.0 V vs SHE (orange dotted line) would be possible. Nevertheless, this ring potential has to be further adjusted depending on the oxidation of the used compound.
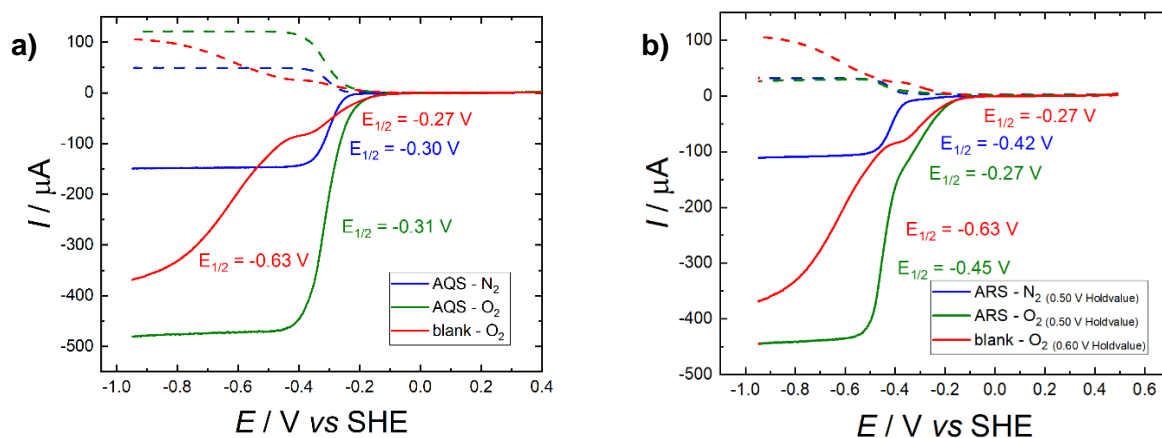
Figure 36: LSV curves at 900 rpm under N_2 conditions versus O_2 conditions in comparison to blank GC in pH 7 under O_2 a) of 1 mM AQS b) of 1mM ARS.

As shown in Figure 36a, the reduction onset potential of AQS in O_2 environment is slightly anodically shifted and the current is increased compared to the LSV graph under N_2. Those LSV graphs of AQS match with literature graphs [45]. The onset as well as the half-wave potential of the ARS reduction remains the same when changing from N_2 to O_2 environment, but the current is more negative under O_2 conditions. In comparison to pH 13, an anodic shift of both compounds can be observed. In addition, ARS dissolved in PB with pH 7 has less reductive steps than in NaOH with pH 13 (Figure 33). This is because in pH 13 the fully deprotonated species is present, whereas only one OH-group is deprotonated in pH 7 [90].

As already mentioned, for ARS only disc excess current values were determined. In order to assess the catalytic effect, the respective excess currents for AQS and ARS in pH 7 are shown in Figure 37. Furthermore, the efficiency of AQS at various rotational rates is displayed in Figure 38.
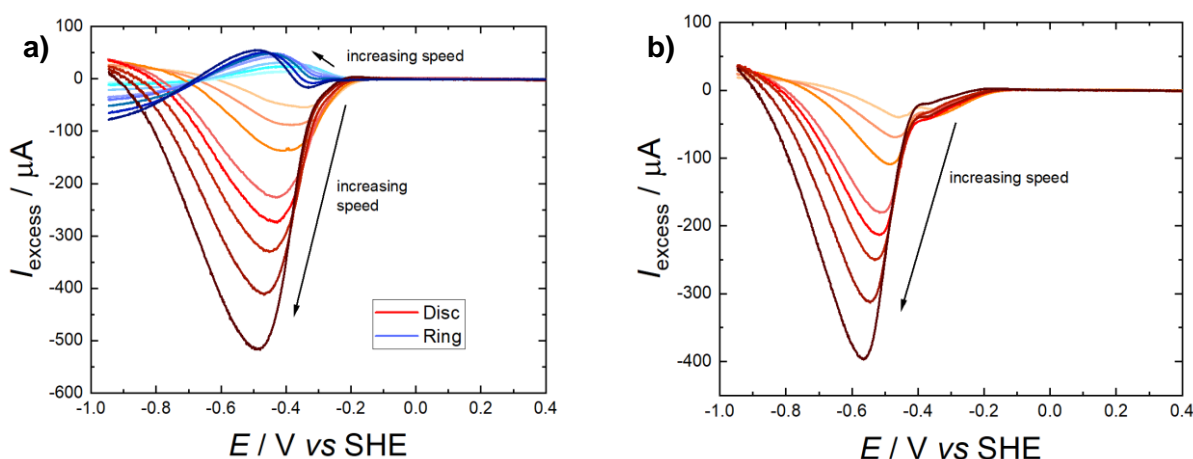
Figure 37: Excess currents at different rotation speeds a) of AQS in pH 7. b) ARS in pH 7.
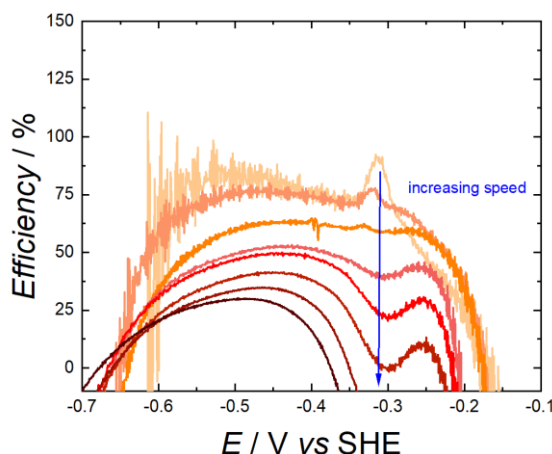
Figure 38: Efficiency of 1 mM ARS in pH 7 at
different rotational rates.

As seen in Figure 37, the two AQ derivatives behave similarly regarding the excess current. However, ARS has less negative current values and both its maximum and onset are at more negative potentials. When comparing the potential of the maximum in pH 13 (-0.47 V vs SHE) with pH 7 (-0.48 V vs SHE), a neglectable difference is noticeable. The maximal excess current is also similar (-491 µA for pH 13 versus -517 µA for pH 7). Additionally, the excess current findings of AQS in pH 7 are in agreement with literature [45]. Interestingly, the efficiency plot shows negative percentage values before and after the catalytic range. There are minima peaks at -0.30 V vs SHE for rotation speeds higher than 200 rpm, whereas the efficiency curves at 100 rpm and 200 rpm have maxima at -0.32 V vs SHE. This is similar to the reported RRDE study of AQS in PB by Wielend *et al.* but the shape of the efficiency curve differs from literature [45].

3.5. Comparison of different anthraquinone derivatives based on chronoamperometric measurements

An additional study of the catalytic activity of the AQ molecules can be done via chronoamperometric measurements. In this approach, the generated amount of H_2O_2 through an electrolysis was measured over time. The produced moles of H_2O_2 and the faradaic efficiencies (FE) based on the calibration data and Eq. 18 respectively were determined and are visually summarized in Figure 39.
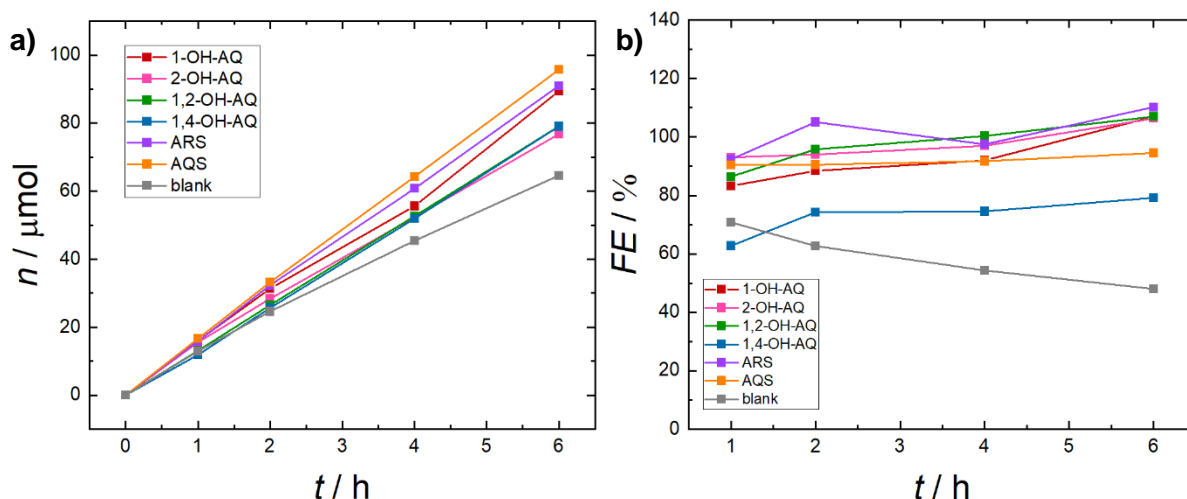
Figure 39: a) Comparison of moles of H_2O_2 produced using different AQ molecules. b) Comparison of faradaic efficiencies (FE) of several AQ derivatives. (Determined through chronoamperometric experiments)

It is obvious that AQS is the compound with the highest amount of moles produced, followed by ARS and 1-OH-AQ. 2-OH-AQ, 1,2-OH-AQ and 1,4-OH-AQ have nearly the same numbers of moles which lie between the blank and the derivatives already mentioned. Nevertheless, the FE data reveals that 1,4-OH-AQ shows the lowest efficiency, whereas 1,2-OH-AQ counts to the compounds with the highest FE-values. Although AQS seems to have the most catalytic effect according to the moles, its FE suggests a lower catalytic efficiency. After 1,4-OH-AQ, the presumed best catalyst AQS shows the next lowest efficiency. On the other hand, ARS has both a high number of moles and high FE. As it can be seen in Figure 39, the electrocatalytic activity of the monohydroxy-substituted AQ derivatives was substantiated. However, 1-OH-AQ increases the amount of produced H_2O_2 more efficiently than 2-OH-AQ but the FE of 2-OH-AQ surpasses the efficiency of 1-OH-AQ. Furthermore, it can be seen that 2-OH-AQ and 1,2-OH-AQ, substances with OH-groups substituted at the position 2, behave very alike. These produce a low molar amount but with a high FE. The AQs with hydroxy-groups at position 1 and 4 show no significant similarities. However, also a trend concerning the number of OH-substituents can be observed. Figure 39 suggests better catalytic performances for monohydroxy-AQ than for dihydroxylated AQ compounds. In comparison to the blank GC measurement in 0.1 M NaOH whose FE decreases over time, an increase in FE of the AQ molecules was observed. In addition, all investigated compounds act catalytically in comparison to the blank GC.

Another comparable parameter for the catalytic influence on the H_2O_2 production by reduction of O_2, presented in Figure 40, is the mean FE of each compound. This diagram demonstrates the high catalytic efficiency of ARS and proves the catalytic activity of 1-OH-AQ, 2-OH-AQ and 1,2-OH-AQ. In contrast to the least observable effect for 1,4-OH-AQ, also AQS acts as a good catalyst.
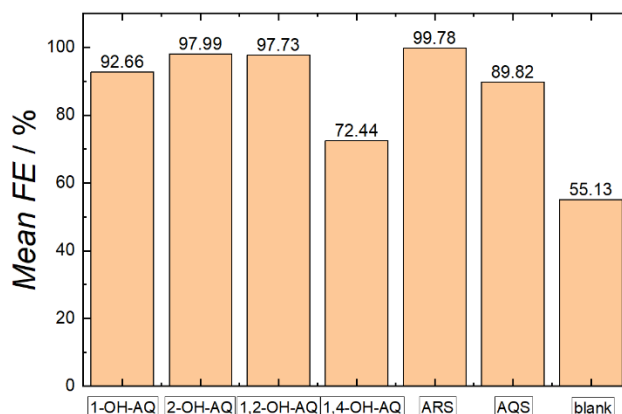
Figure 40: Bar diagram of the mean faradaic efficiencies (FE) determined through chronoamperometric experiments, comparison of various AQ derivatives with blank GC.

As already mentioned in chapter 2.4.3., samples of 0.3 mM AQ derivative solutions in 0.1 M NaOH were taken during the chronoamperometric measurement between 0 h and 6 h to monitor the production of H_2O_2. Subsequently, the H_2O_2 detection was performed via UV-Vis spectroscopy. In Figure 41, the delta absorbance spectra of those samples of 1,2-OH-AQ are displayed. These spectra reveal a H_2O_2 peak at 413 nm which is increasing with electrolysis time. This increase indicates a successful H_2O_2 production. No additional peak corresponding to the AQ molecule is visible. Similar to Figure 41, the increasing H_2O_2 maximum at 413 nm was also detected in the spectra of all other AQ compounds. Additionally, the respective AQ peaks are not visible in most of those delta absorbance spectra. The only AQ derivative with an observable peak is 1,4-OH-AQ. In chapter 3.1.4., the decrease of 1,4-OH-AQ with electrolysis time was already shown in Figure 19.
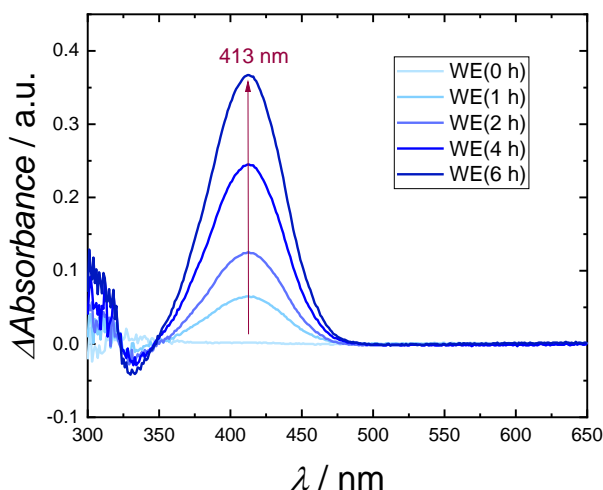
Figure 41: Delta absorbance spectra of H_2O_2 detection of 0.3 mM 1,2-OH-AQ in 0.1 M NaOH.

3.6. RRDE method compared to chronoamperometric results

Due to the use of the RRDE method as well as chronoamperometric experiments, the results of those two different analysis approaches concerning the electrocatalytic behavior of the studied AQ derivatives can also be compared. Hence, the mean FE was plotted against the onset potential of the excess current (Figure 42).
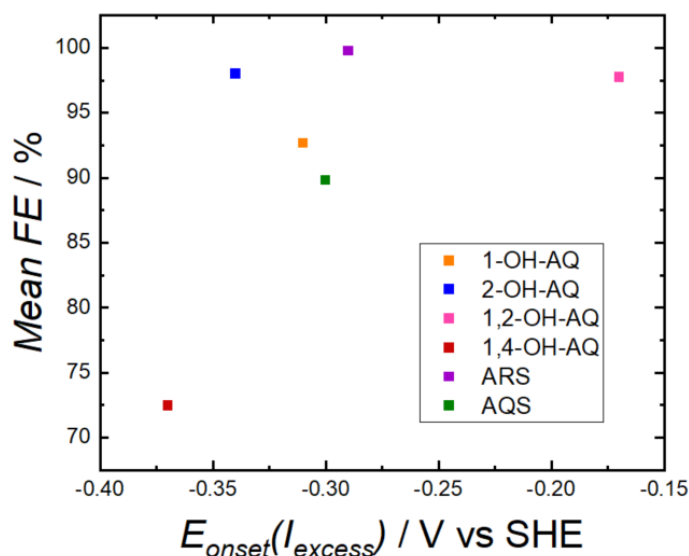
Figure 42: Mean FE calculated via chronoamperometric measurements as a function of the onset potential determined through the RRDE method.

According to Figure 42, 1,2-OH-AQ has not only the earliest catalytic effect due to the lowest onset of the excess current, but also shows one of the highest mean FE-values. Nevertheless, the impossibility of using the RRDE method with 1,2-OH-AQ in pH 13 because of its low oxidation onset potential has to be taken into account. Additionally, the comparison of both methods reveals again the low catalytic activity of 1,4-OH-AQ. Moreover, a slight trend can be observed. The decrease of the onset potential seems to relate to an increase of the mean FE.

As shown in Table 8, there would be more possible parameters and data to compare. Nevertheless, further comparisons turned out to be difficult without linear correlation. RRDE experiments and chronoamperometry are two different methods to investigate the electrocatalysis regarding ORR. Therefore, they are complementary and cannot be compared that easily. On the one side, RRDE systems are based on the rotation resulting in the electron transfer on the electrodes. The products formed at the GC disc electrode are moved towards the Pt ring where these are re-oxidized using a constant ring potential. Thus, the RRDE results depend on the applied Pt ring potential, the rotational rate and the electrode design. If the same parameters are used for all measurements, the electrocatalytic effect of different AQ derivatives can be qualitatively analyzed. On the other hand, chronoamperometric experiments are performed by applying a constant potential at the GC electrode. Thereby, the current-time dependence can be recorded. Additionally, the H_2O_2 detection of intermittently taken samples enables a time dependent quantification of the produced H_2O_2. Due to the application of the same constant GC potential for all electrolysis, a difference in the overpotential can be assumed. Both techniques are diffusion-limited. However, the different operating principles of the two methods yield different data with various dependencies. Therefore, the comparison of the RRDE method with chronoamperometry is currently impeded. Future research work might enable the comparability.

4. Conclusion

In this thesis, the electrocatalytic activity of various homogenously dissolved anthraquinone (AQ) derivatives towards the hydrogen peroxide (H_2O_2) production via the oxygen (O_2) reduction was investigated. As the qualitative observations through cyclic voltammetry (CV) were insufficient to

scientifically prove the catalytic behavior, rotating ring-disc electrode (RRDE) measurements and chronoamperometric experiments were performed.

With regard to the RRDE method, the major disadvantage is the requirement of a suitable ring potential at a Pt ring. Thus, the further oxidation of 1,2-dihydroxyanthraquinone and 1,4-dihydroxyanthraquinone prevented the complete use of the Pt ring electrode. If a possible potential is found, the RRDE experiments enable a fast determination of excess currents and efficiencies. This allows the assessment whether a substance acts as a catalyst. In this manner, it was proven that all investigated AQ compounds in NaOH with pH 13 show a catalytic effect over blank GC. Especially anthraquinone 2-sulfonate enhances the two-electron O_2 reduction to a great extent. In contrast, the RRDE results suggest a lower electrocatalytic activity of the dihdroxy-AQs. However, 1,2-dihydroxyanthraquinone has an exceptional low onset potential of the excess current. The catalytic behavior of Alizarin Red S, 1-hydroxyanthraquinone and 2-hydroxyanthraquinone is in between.

Alternatively, the generated H_2O_2 can be quantified by electrolysis of the AQ derivatives dissolved in NaOH (pH 13). There are no limitations concerning oxidation potentials, but chronoamperometry is a time-consuming tool to investigate the electrocatalysis. The higher amount of H_2O_2 and higher faradaic efficiency (FE) compared to the blank glassy carbon (GC) electrode verify that the analyzed AQ derivatives catalyze the H_2O_2 production. In comparison to all other compounds, 1,4-dihydroxyanthraquinone produced a low number of moles and showed a low FE. Although the considerable H_2O_2 amount using anthraquinone 2-sulfonate is in accordance with the RRDE technique, its FE contradicts the assumption of being the most appropriate catalyst. Due to the findings, Alizarin Red S can be suspected to facilitate the reduction of O_2 overall the most regarding the electrolysis experiments. Additionally, the high FE of 1,2-dihydroxyanthraquinone is also remarkable considering its lower amount of H_2O_2. Again, 1-hydroxyanthraquinone and 2-hydroxyanthraquinone prove to be suitable but moderate electrocatalysts.

In conclusion, RRDE experiments and chronoamperometric measurements are two possible but complementary methods for the electrochemical study of the catalytic behavior of anthraquinone derivatives towards the two-electron O_2 reduction. Both yield qualitatively similar results and the comparison of the two different approaches suggests a connection between faradaic efficiency and onset potential of the excess current but quantitative comparison tools and methods still require further research.

5. Appendix
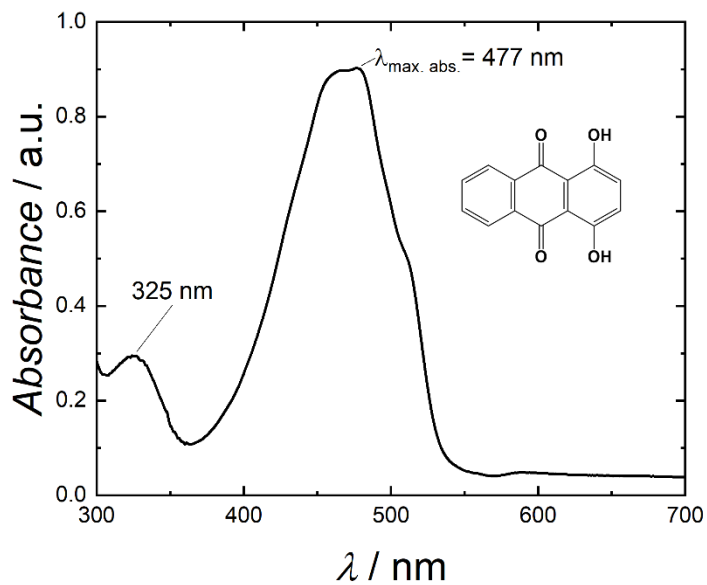
Figure 43: UV-Vis absorbance spectrum of a 0.1 mM solution of 1,4-OH-AQ in MeCN.
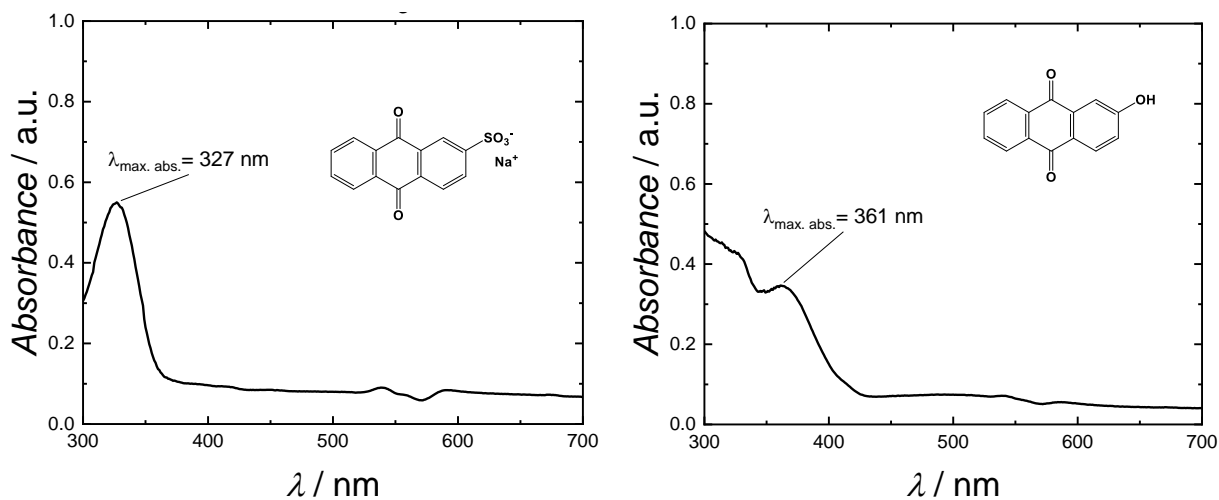
Figure 44: UV-Vis absorbance spectrum of a 0.1 mM solution in MeCN of a) AQS b) 2-OH-AQ.
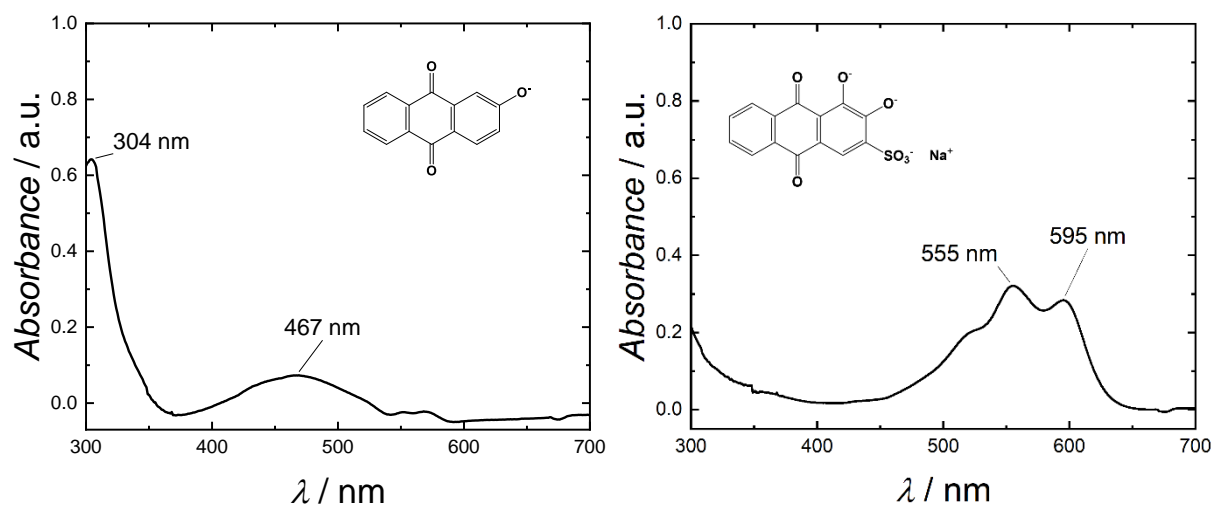
Figure 45: UV-Vis absorbance spectrum of a 0.025 mM solution in 0.1 M NaOH of a) 2-OH-AQ b) ARS.
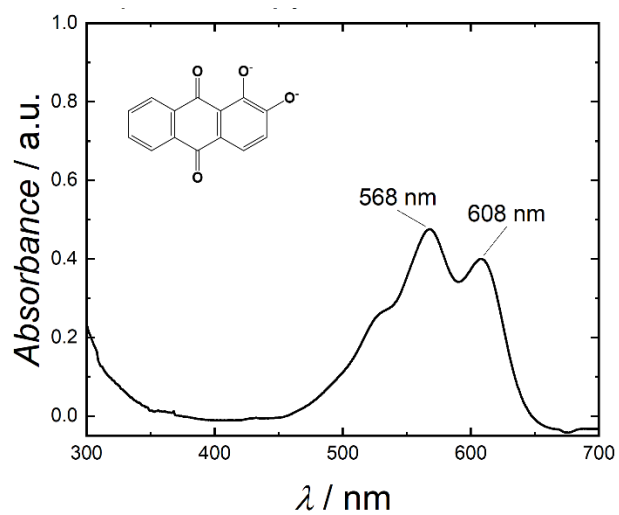
Figure 46: UV-Vis absorbance spectrum of a 0.025 mM solution of 1,2-OH-AQ in 0.1 M NaOH.
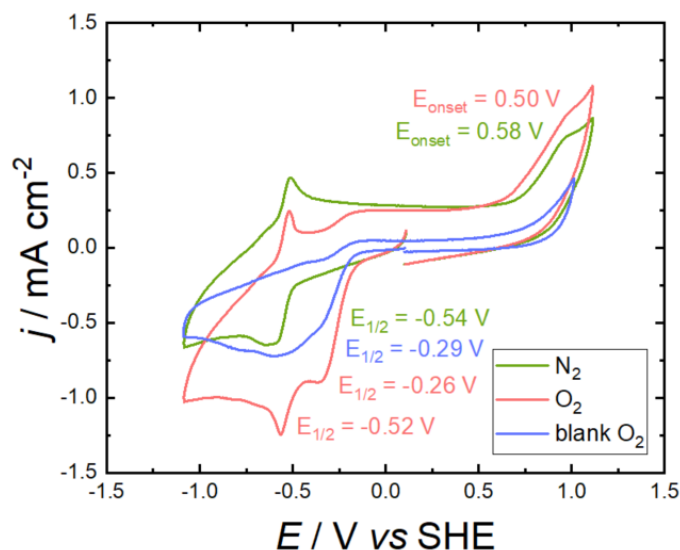
Figure 47: CV of 0.4 mM 1-OH-AQ in 0.1 M NaOH under N_2 and O_2 condition versus blank GC under O_2.
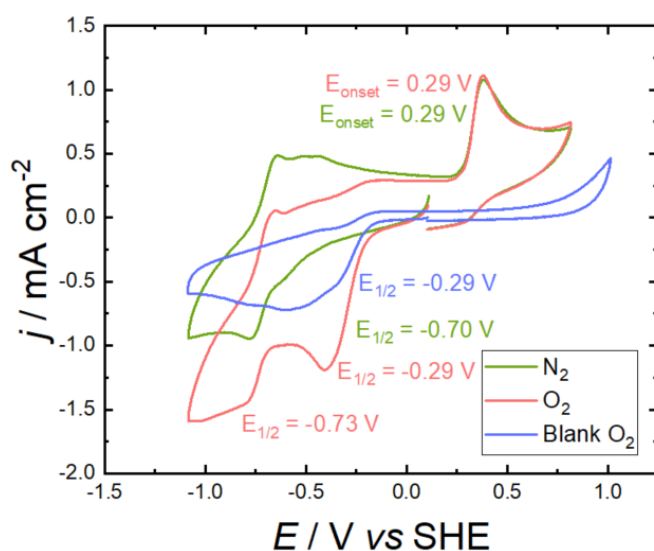
Figure 48: CV of 1 mM ARS in 0.1 M NaOH under N_2 and O_2 condition versus blank GC under O_2.

6. References

[1] T. Kousksou, P. Bruel, A. Jamil, T. El Rhafiki, Y. Zeraouli, *Sol. Energy Mater. Sol. Cells* **2014**, *120*, 59.

[2] A. Poullikkas, *Renewable Sustainable Energy Rev.* **2007**, *11*, 30.

[3] S. Fukuzumi, Y. Yamada, K. D. Karlin, *Electrochimica Acta* **2012**, *82*, 493.

[4] G. Goor, J. Glenneberg, S. Jacobi, J. Dadabhoy, E. Candido, in *Ullmann's Encyclopedia of Industrial Chemistry* (Eds.: G. Goor, J. Glenneberg, S. Jacobi, J. Dadabhoy, E. Candido), Wiley-VCH Verlag GmbH & Co. KGaA. Weinheim, Germany **2000**, p. 1.

[5] Y. Lu, A. Sehrish, R. Manzoor, K. Dong, Y. Jiang, *Chem Rep* **2019**, *1*, 81.

[6] N. S. Davis, J. H. Keefe, *Ind. Eng. Chem.* **1956**, *48*, 745.

[7] J. M. Campos-Martin, G. Blanco-Brieva, J. L. G. Fierro, *Angew. Chem., Int. Ed.* **2006**, *45*, 6962.

[8] R. Dittmeyer, J.-D. Grunwaldt, A. Pashkova, *Catal. Today* **2015**, *248*, 149.

[9]   T. Nishimi, T. Kamachi, K. Kato, T. Kato, K. Yoshizawa, *Eur. J. Org. Chem.* **2011**, *2011*, 4113.

[10] S. C. Perry, D. Pangotra, L. Vieira, L.-I. Csepei, V. Sieber, L. Wang, C. Ponce de León, F. C. Walsh, *Nat Rev Chem* **2019**, *3*, 442.

[11] S. C. Perry, S. Mavrikis, L. Wang, C. Ponce de León, *Curr. Opin. Electrochem.* **2021**, *30*, 100792.

[12] C. Samanta, *Appl. Catal., A* **2008**, *350*, 133.

[13] J. K. Edwards, G. J. Hutchings, *Angew. Chem., Int. Ed.* **2008**, *47*, 9192.

[14] K. Kosaka, H. Yamada, K. Shishida, S. Echigo, R. A Minear, H. Tsuno, Matsui, Saburo, *Water Res.* **2001**, *35*, 3587.

[15] A. Goi, M. Trapido, N. Kulik, *Int. J. Chem. Mol. Eng.* **2009**, *3*, 209.

[16] O. V. Romantsova, V. B. Ulybin, *Acta Astronaut.* **2015**, *109*, 231.

[17] J. D. Clark, *Ignition!: An Informal History of Liquid Rocket Propellants*, Rutgers University Press, New Jersey **1972**.

[18] W. Kopacz, A. Okninski, A. Kasztankiewicz, P. Nowakowski, G. Rarata, P. Maksimowski, *FirePhysChem* **2022**, *2*, 56.

[19] R. Goyal, O. Singh, A. Agrawal, C. Samanta, B. Sarkar, *Catalysis Rev.* **2020**.

[20] A. E. Sanli, A. Aytaç, *Int. J. Hydrogen Energy* **2011**, *36*, 869.

[21] S. Yamazaki, Z. Siroma, H. Senoh, T. Ioroi, N. Fujiwara, K. Yasuda, *J. Power Sources* **2008**, *178*, 20.

[22] E. C. Murphy, A. J. Friedman, *J. Am. Acad. Dermatol.* **2019**, *81*, 1379.

[23] K. Izu, O. Yamamoto, M. Asahi, *Dermatology (Basel, Switz.)* **2000**, *201*, 61.

[24] L. J. Thénard, *Ann. Chim. Phys.* **1818**, *8*, 306.

[25] C. W. Jones, *Applications of Hydrogen Peroxide and Derivatives*, The Royal Society of Chemistry, Cambridge **1999**.

[26] H. Meidinger, *Justus Liebigs Ann. Chem.* **1853**, *88*, 57.

[27] W. Manchot, *Justus Liebigs Ann. Chem.* **1901**, *314*, 177.

[28] H.-J. Riedl, G. Pfleiderer, *Preparation from organic compounds by the alkyl-anthraquinone process: US Patent* **1939**.

[29] R. Edvinsson Albers, M. Nyström, M. Siverström, A. Sellin, A.-C. Dellve, U. Andersson, W. Herrmann, T. Berglin, *Catal. Today* **2001**, *69*, 247.

[30] Y. Hou, Y. Wang, F. He, S. Han, Z. Mi, W. Wu, E. Min, *Mater. Lett.* **2004**, *58*, 1267.

[31] G. Blanco-Brieva, F. Desmedt, P. Miquel, J. M. Campos-Martin, J. L. G. Fierro, *Catal. Sci. Technol.* **2020**, *10*, 2333.

[32] H. Henkel, W. Weber, *Manufacture of hydrogen peroxid: US Patent* **1914**.

[33] Y. Sun, I. Sinev, W. Ju, A. Bergmann, S. Dresp, S. Kühl, C. Spöri, H. Schmies, H. Wang, D. Bernsmeier, B. Paul, R. Schmack, R. Kraehnert, B. Roldan Cuenya, P. Strasser, *ACS Catal.* **2018**, *8*, 2844.

[34] C. H. Choi, H. C. Kwon, S. Yook, H. Shin, H. Kim, M. Choi, *J. Phys. Chem. C* **2014**, *118*, 30063.

[35] J. Park, Y. Nabae, T. Hayakawa, M. Kakimoto, *ACS Catal.* **2014**, *4*, 3749.

[36] I. Yamanaka, S. Tazawa, T. Murayama, T. Iwasaki, S. Takenaka, *ChemSusChem* **2010**, *3*, 59.

[37] A. Kulkarni, S. Siahrostami, A. Patel, J. K. Nørskov, *Chem. Rev.* **2018**, *118*, 2302.

[38] C. Song, J. Zhang, in *PEM Fuel Cell Electrocatalysts and Catalyst Layers* (Ed.: J. Zhang), Springer London. London **2008**, p. 89.

[39] J. K. Nørskov, J. Rossmeisl, A. Logadottir, L. Lindqvist, J. R. Kitchin, T. Bligaard, H. Jónsson, *J. Phys. Chem. B* **2004**, *108*, 17886.

[40] K. Tammeveski, K. Kontturi, R. J. Nichols, R. J. Potter, D. J. Schiffrin, *J. Electroanal. Chem.* **2001**, *515*, 101.

[41] A. Sarapuu, K. Vaik, D. J. Schiffrin, K. Tammeveski, *J. Electroanal. Chem.* **2003**, *541*, 23.

[42] K. Vaik, U. Mäeorg, F. C. Maschion, G. Maia, D. J. Schiffrin, K. Tammeveski, *Electrochim. Acta* **2005**, *50*, 5126.

[43] K. Vaik, D. J. Schiffrin, K. Tammeveski, *Electrochem. Commun.* **2004**, *6*, 1.

[44] K. Vaik, A. Sarapuu, K. Tammeveski, F. Mirkhalaf, D. J. Schiffrin, *J. Electroanal. Chem.* **2004**, *564*, 159.

[45] D. Wielend, H. Neugebauer, N. S. Sariciftci, *Electrochem. Commun.* **2021**, *125*, 106988.

[46] E. Leeb, D. Wielend, C. Schimanofsky, N. S. Sariciftci, *Electrochem. Science Adv.* **2022**.

[47] H. Rabl, D. Wielend, S. Tekoglu, H. Seelajaroen, H. Neugebauer, N. Heitzmann, D. H. Apaydin, M. C. Scharber, N. S. Sariciftci, *ACS Appl. Energy Mater.* **2020**, *3*, 10611.

[48] D. H. Apaydin, H. Seelajaroen, O. Pengsakul, P. Thamyongkit, N. S. Sariciftci, J. Kunze-Liebhäuser, E. Portenkirchner, *ChemCatChem* **2018**, *10*, 1793.

[49] M. Jakešová, D. H. Apaydin, M. Sytnyk, K. Oppelt, W. Heiss, N. S. Sariciftci, E. D. Głowacki, *Adv. Funct. Mater.* **2016**, *26*, 5248.

[50] V. G. Levich, in *Prentice-Hall International Series in the Physical and Chemical Engineering Sciences* (Ed.: N. R. Amundson), Prentice-Hall. Englewood Cliffs **1962**.

[51] F. Dalton, *Trans. Electrochem. Soc.* **2016**, *25*, 50.

[52] A. Alexiadis, A. Cornell, M. P. Dudukovic, *J. Electroanal. Chem.* **2012**, *669*, 55.

[53] A. J. Bard, L. R. Faulkner, *Electrochemical Methods: Fundamentals and Applications*, John Wiley & Sons, New York **2001**.

[54] U. A. Paulus, T. J. Schmidt, H. A. Gasteiger, R. J. Behm, *J. Electroanal. Chem.* **2001**, *495*, 134.

[55] D. Wielend, *Electrochemical H_2O_2 production using immoblized organic catalysts*, Linz **2021**.

[56] O. Antoine, R. Durand, *J. Appl. Electrochem.* **2000**, *30*, 839.

[57] W. J. Albery, Hitchman M. L., *Ring-Disc Electrodes*, Clarendon Press, Oxford **1971**.

[58] P. Manisankar, A. Gomathi, *J. Mol. Catal. A: Chem.* **2005**, *232*, 45.

[59] M. R. Gerhardt, L. Tong, R. Gómez-Bombarelli, Q. Chen, M. P. Marshak, C. J. Galvin, A. Aspuru-Guzik, R. G. Gordon, M. J. Aziz, *Adv. Energy Mater.* **2017**, *7*, 1601488.

[60] J. E. Bachman, L. A. Curtiss, R. S. Assary, *J. Phys. Chem. A* **2014**, *118*, 8852.

[61] C. Schimanofsky, *(Spectro)electrochemical investigation of anthraquinone derivatives under CO_2 and O_2*, Linz **2021**.

[62] D. O. Andersen, N. D. Weber, S. G. Wood, B. G. Hughes, B. K. Murray, J. A. North, *Antiviral Res.* **1991**, *16*, 185.

[63] G. K. Panigrahi, A. Yadav, P. Mandal, A. Tripathi, M. Das, *Toxicol. Lett.* **2016**, *245*, 15.

[64] A. D. Kshirsagar, P. V. Panchal, U. N. Harle, R. K. Nanda, H. M. Shaikh, *Int. J. Inflammation* **2014**, *2014*, 690596.

[65] P. Khanal, B. M. Patil, J. Chand, Y. Naaz, *Nat. Prod. Bioprospect.* **2020**, *10*, 325.

[66] E. M. Malik, C. E. Müller, *Med. Res. Rev.* **2016**, *36*, 705.

[67] P. L. Chesis, D. E. Levin, M. T. Smith, L. Ernster, B. N. Ames, *Proc. Natl. Acad. Sci. U. S. A.* **1984**, *81*, 1696.

[68] G. Minotti, P. Menna, E. Salvatorelli, G. Cairo, L. Gianni, *Pharmacol. Rev.* **2004**, *56*, 185.

[69] T. J. Monks, R. P. Hanzlik, G. M. Cohen, D. Ross, D. G. Graham, *Toxicol. Appl. Pharmacol.* **1992**, *112*, 2.

[70] Y. Caro, L. Anamale, M. Fouillaud, P. Laurent, T. Petit, L. Dufosse, *Nat. Prod. Bioprospect.* **2012**, *2*, 174.

[71] L. Dufossé, *Food Res. Int.* **2014**, *65*, 132.

[72] H. Rabl, *Electrochemical oxygen reduction to hydrogen peroxide using conducting polymers*, Linz **2020**.

[73] N. Elgrishi, K. J. Rountree, B. D. McCarthy, E. S. Rountree, T. T. Eisenhart, J. L. Dempsey, *J. Chem. Educ.* **2018**, *95*, 197.

[74] N. G. Connelly, W. E. Geiger, *Chem. Rev.* **1996**, *96*, 877.

[75] P. G. Gassman, C. H. Winter, *J. Am. Chem. Soc.* **1986**, *108*, 4228.

[76] G. Su, Y. Wei, M. Guo, *Am. J. Anal. Chem.* **2011**, *02*, 879.

[77] J. Zhao, S. Xue, J. Barber, Y. Zhou, J. Meng, X. Ke, *J. Mater. Chem. A* **2020**, *8*, 4700.

[78] D. Ajloo, B. Yoonesi, A. Soleymanpour, *Int. J. Electrochem. Sci.* **2010**, *5*, 459.

[79] H. P. Upadhyaya, *J. Mol. Struct.* **2021**, *1232*, 130050.

[80] Z. Machatová, Z. Barbieriková, P. Poliak, V. Jančovičová, V. Lukeš, V. Brezová, *Dyes Pigm.* **2016**, *132*, 79.

[81] K. Itoh, Y. Kitade, C. Yatome, *Bull. Environ. Contam. Toxicol.* **1998**, *60*, 786.

[82] D. Deng, J. Guo, G. Zeng, G. Sun, *Int. Biodeterior. Biodegrad.* **2008**, *62*, 263.

[83] K. Itoh, C. Yatome, T. Ogawa, *Bull. Environ. Contam. Toxicol.* **1993**, *50*, 522.

[84] J. Zhang, Y. Chi, L. Feng, *BMC Biotechnol.* **2021**, *21*, 64.

[85] A. Boonyakamol, T. Imai, P. Chairattanamanokorn, T. Higuchi, M. Sekine, *Appl. Biochem. Biotechnol.* **2009**, *158*, 180.

[86] M. Shamsipur, A. Siroueinejad, B. Hemmateenejad, A. Abbaspour, H. Sharghi, K. Alizadeh, S. Arshadi, *J. Electroanal. Chem.* **2007**, *600*, 345.

[87] A. Ashnagar, J. Bruce, P. Dutton, R. C. Prince, *Biochim. Biophys. Acta, Gen. Subj.* **1984**, *801*, 351.

[88] Z. J. Zhang, X. Y. Chen, *Electrochim. Acta* **2018**, *282*, 563.

[89] T. Kasa, T. Solomon, *Am. J. Phys. Chem.* **2016**, *5*, 45.

[90] A. A. Shalaby, A. A. Mohamed, *RSC Adv.* **2020**, *10*, 11311.

7. List of figures

8. List of schemes

9. List of tables